Fault slip rates and interseismic deformation in the western Transverse Ranges, California

Scott T. Marshall,[1] Gareth J. Funning,[2] and Susan E. Owen[3]

Received 6 April 2013; revised 25 July 2013; accepted 27 July 2013.

[1] To better constrain fault slip rates and patterns of interseismic deformation in the western Transverse Ranges of southern California, we present results from analysis of GPS and interferometric synthetic aperture radar (InSAR) data and three-dimensional mechanical and kinematic models of active faulting. Anthropogenic motions are detected in several localized zones but do not significantly affect the vast majority of continuous GPS site locations. GPS measures contraction rates across the Ventura Basin of ~7 mm/yr oriented west-northwest with rates decreasing to the west and east. The Santa Barbara channel is accommodating ~6.5 mm/yr in the east and ~2.5 mm/yr in the western portions of N/S contraction. Inversion of horizontal GPS velocities highlights a zone of localized fast contraction rates following the Ventura Basin. Using a mechanical model driven by geodetically calculated strain rates, we show that there are no significant discrepancies between short-term slip rates captured by geodesy and longer-term slip rates measured by geology. Mechanical models reproduce the first-order interseismic velocity and strain rate patterns but fail to reproduce strongly localized contraction in the Ventura Basin due to the inadequate homogeneous elastic properties of the model. Existing two-dimensional models match horizontal rates but predict significant uplift gradients that are not observed in the GPS data. Mechanical models predict zones of fast contraction in the Santa Barbara channel and offshore near Malibu, suggesting that offshore faults represent a significant seismic hazard to the region. Furthermore, many active faults throughout the region may produce little to no interseismic deformation, making accurate seismic hazard assessment challenging.

Citation: Marshall, S. T., G. J. Funning, and S. E. Owen (2013), Fault slip rates and interseismic deformation in the western Transverse Ranges, California, *J. Geophys. Res. Solid Earth*, *118*, doi:10.1002/jgrb.50312.

1. Introduction

[2] Much effort has been devoted to preparing for the next large ~M>7.5 strike-slip earthquake along the San Andreas fault in southern California [e.g., *Field et al*., 2007]; however, moderate to large events (M6.5–M7.5) occurring along smaller faults near population centers could be equally or, in some cases, more devastating [e.g., *Dolan et al*., 1995]. For example, the 1994 M6.7 Northridge earthquake ruptured a ~30 km long and previously unrecognized blind thrust and was one of the most expensive natural disasters in the history of the United States [*Scientists of the U.S. Geologic Survey* (*USGS*) *and the Southern California Earthquake Center* (*SCEC*), 1994]. Accurate seismic hazard assessments require detailed knowledge of fault parameters, including fault geometry and slip rates, and these parameters can be estimated from space geodetic data when combined with various forms of computational fault modeling.

[3] Geodetic measurements have long been used to estimate surface strain and fault slip rates in regions of active faulting [*Freund and Barnett*, 1976; *Savage and Burford*, 1970, 1973]. Modern satellite geodesy therefore offers a complementary toolset to seismic hazard assessments because fault locations, geometries, and slip rates can be constrained by geodetic data. Unfortunately, because short, slow slip rate, and/or deeply locked faults produce relatively small surface deformations during the interseismic period, interseismic geodetic data have been most commonly utilized to understand relatively long, fast-slipping faults, with relatively shallow slip [e.g., *Bürgmann et al*., 2002; *McCaffrey*, 2005; *Meade et al*., 2002; *Savage and Burford*, 1973; *Savage and Lisowski*, 1998; *Savage et al*., 1999; *Schmalzle et al*., 2006]. Furthermore, due to the mathematical trade-offs between slip rate and locking depths, especially for closely spaced faults [e.g., *Platt and Becker*, 2010], performing mathematical inversions for fault parameters always yields nonunique and potentially unreliable results. Thus, from a satellite geodesy perspective, slow-moving and/or short

Additional supporting information may be found in the online version of this article.

[1]Department of Geology, Appalachian State University, Boone, North Carolina, USA.
[2]Department of Earth Sciences, University of California, Riverside, California, USA.
[3]Jet Propulsion Laboratory, Pasadena, California, USA.

Corresponding author: S. T. Marshall, Department of Geology, Appalachian State University, 572 Rivers Street, Boone, NC 28608, USA. (marshallst@appstate.edu)

2169-9313/13/10.1002/jgrb.50312

Table 1. Existing Geologic Reverse Slip Rate Estimates for the Western Transverse Ranges Region

Fault Name	Slip Rate (mm/yr)	Reference
Holser	0–0.4	*Peterson et al*. [1996]
Mission Ridge/Arroyo Parida	0.35–1.27	*Rockwell et al*. [1984] (assuming a sum of vert uplift on Oak View faults)
Northridge	0.35–1.7	Low: *Dolan et al*. [1997]; High: *Davis and Namson* [1994]; *Huftile and Yeats* [1996]
Northridge Hills	0.3–1.7	*Baldwin et al*. [2000]
Oak Ridge Onshore	1.7–5.0	*Huftile and Yeats* [1996]
Red Mountain	0.31–7.16	*Huftile and Yeats* [1995]
San Cayetano	1.03–10.7	*Rockwell* [1988]; *Huftile and Yeats* [1996]
Santa Monica	0.5–5.9	Low: *Dolan and Pratt* [1997]; High: *Davis and Namson* [1994]
Santa Susana	2.1–9.8	*Huftile and Yeats* [1996]
Sierra Madre	0.6–5.0	Low: *Tucker and Dolan* [2001]; *Rubin et al*. [1998]; High: *Tucker and Dolan* [2001]
Simi	0.4–0.9	Low: *Hitchcock* [2001] High: *Gonzalez and Rockwell* [1991]
Ventura	0.8–2.4	*Peterson and Wesnousky* [1994]

faults are relatively poorly characterized compared to longer and faster-slipping faults. Consequently, a relative lack of knowledge of the hazards of small and slowly slipping fault structures is a shortcoming in current seismic hazard assessments.

[4] In this work, we use continuous Global Positioning System (GPS) data from the Plate Boundary Observatory (PBO) along with interferometric synthetic aperture radar (InSAR) data to determine the patterns of anthropogenic, seasonal, and tectonic deformation throughout the western Transverse Ranges. We use a three-dimensional mechanical fault model incorporating the finite and nonplanar fault surfaces defined by the Southern California Earthquake Center (SCEC) Community Fault Model (CFM) to simulate both long-term and interseismic deformation rates. We compare model results to long-term geologic slip rate estimates as well as the current tectonic geodetic velocities and deformation rates. Because this technique does not rely on directly inverting the geodetic data for fault parameters and produces kinematically and mechanically viable slip rates and distributions, it is well suited to determine the partitioning of slip among the diffuse network of slowly slipping and highly segmented active faults in the western Transverse Ranges of southern California.

2. Existing Interseismic Deformation Models of the Western Transverse Ranges

[5] The regional-scale left step in the San Andreas fault (i.e., the Big Bend) results in ongoing contraction throughout the Transverse Ranges of southern California. A complex geologic history of Miocene extension, followed by recent and ongoing transpression, has resulted in a complex network of oblique-slip, strike-slip, and reverse faults (Figure 1) that now accommodate localized shortening across the Ventura Basin [e.g., *Donnellan et al*., 1993a; *Donnellan et al*., 1993b; *Huftile and Yeats*, 1995; *Tsutsumi and Yeats*, 1999; *Wright*, 1991]. Due to a wealth of borehole data, the subsurface fault geometries of the region are relatively well constrained [e.g., *Davis and Namson*, 1989, 1994; *Huftile and Yeats*, 1994, 1995, 1996; *Namson and Davis*, 1988; *Tsutsumi and Yeats*, 1999; *Yeats*, 1987; *Yeats et al*., 1988], and many faults exhibit complex nonplanar surfaces [e.g., *Carena and Suppe*, 2002; *Çemen*, 1989; *Plesch et al*., 2007; *Yeats*, 1987; *Yeats et al*., 1987]. While numerous geologic estimates of fault slip rates exist throughout the region, disparate structural interpretations of borehole data [e.g., *Davis and Namson*, 1994; *Huftile and Yeats*, 1995], large uncertainties in dates of geologic units [e.g., *Yeats*, 1993], and a limited number of paleoseismic [e.g., *Dolan et al*., 2000a; *Rockwell*, 1988] and geomorphologic studies [e.g., *Azor et al*., 2002; *Rockwell et al*., 1984] have resulted in large ranges in existing slip rate estimates (Table 1). Many fault slip rates in the region remain unconstrained. Further complicating the issue, *Marshall et al*. [2008] suggest that the long-term fault slip distributions in the region are rather complex, varying both along-strike and with depth. Thus, existing geologic slip rate estimates in the western Transverse Ranges may have been calculated at locations that are not representative of the fault as a whole.

[6] Despite the abundant evidence for the existence of complex, nonplanar, and segmented faults throughout the western Transverse Ranges, existing models of interseismic deformation in the region use highly simplified two-dimensional or geometrically simple fault geometries [*Becker et al*., 2005; *Donnellan et al*., 1993b; *Hager et al*., 1999; *McCaffrey*, 2005; *Meade and Hager*, 2005]. As a result, these models are not well suited to investigate deformation in regions of finite, nonplanar faults. For example, the Ventura/western Transverse Ranges block, "VENT," in the model of *McCaffrey* [2005] produces a significant portion of the total plate boundary misfit, suggesting that the block assumptions are not well satisfied in the region. This arises, at least in part, from a key assumption of the block modeling approach [e.g., *Becker et al*., 2005; *Loveless and Meade*, 2011; *McCaffrey*, 2005; *Meade and Hager*, 2005] that all blocks are bounded by connected faults. Two-dimensional models of the western Transverse Ranges [*Donnellan et al*., 1993a; *Hager et al*., 1999] implicitly assume that fault traces are infinitely long and planar in the third dimension. These assumptions are inconsistent with field and subsurface data that reveal the finite and nonplanar nature of faults within the Transverse Ranges [e.g., *Carena and Suppe*, 2002; *Huftile and Yeats*, 1995; *Shaw et al*., 2002; *Yeats*, 1988; *Yeats*, 1987].

[7] An alternative approach to modeling interseismic deformation is to use geodetic data to determine a regional strain or shortening rate and then use the regional strain rate to drive deformation in a forward mechanical model [*Cooke and Marshall*, 2006; *Cooke and Dair*, 2011; *Dair and Cooke*, 2009; *Herbert and Cooke*, 2012; *Marshall et al*., 2008, 2009; *Meigs et al*., 2008]. For example, using mechanical models of the western Transverse Ranges, *Marshall et al*. [2008] predict complex secular slip distributions throughout the region, generally in agreement with geologic estimates.

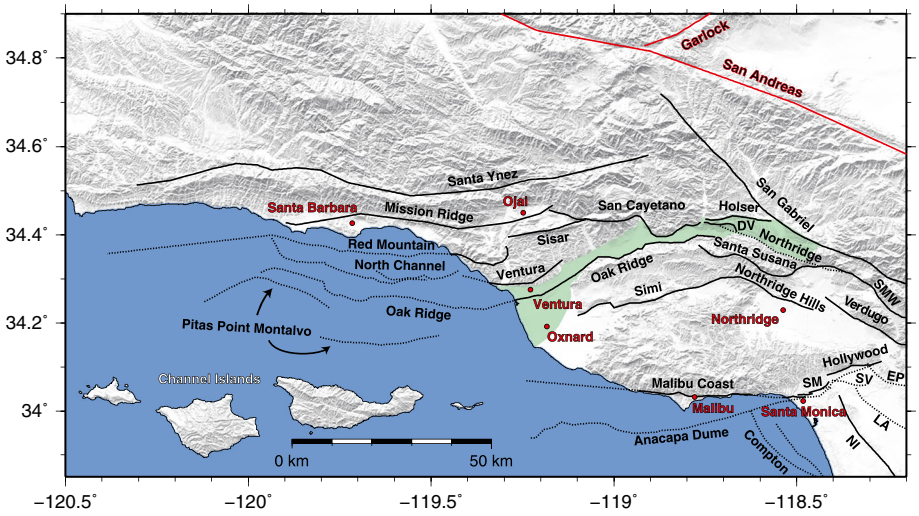

Figure 1. Location map, fault traces, and shaded digital elevation model of the western Transverse Ranges study area. Selected cities are labeled with red circles and text, and a generalized outline of the surface expression of the Ventura Basin is highlighted in green. The Santa Barbara Channel is the region between the Channel Islands and the coast near Santa Barbara. Fault traces included in numerical models are shown with black lines (dotted when offshore or blind) and are based on the Southern California Earthquake Center (SCEC) Community Fault Model (CFM) version 4.0. The San Andreas and Garlock faults are not included in the numerical models presented here but are shown with red lines for reference. Fault abbreviations are as follows: DV, Del Valle; EP, Elysian Park; LA, Los Angeles segment of the Puente Hills thrust; NI, Newport-Inglewood; SM, Santa Monica; SMW, Sierra Madre West; SV, San Vicente. Several faults from the nearby Los Angeles Basin (to the southeast) are included in the numerical models in order to properly account for any potential mechanical interactions between these structures. A complete three-dimensional and interactive version of the modeled fault mesh is provided in the supporting information.

Marshall et al. [2009] use a similar technique to match both geologic slip rates as well as interseismic GPS data in the nearby Los Angeles Basin. In this study, we use the *Marshall et al*. [2009] approach and demonstrate that a forward mechanical modeling approach can successfully match both long-term geologic slip rates and the first-order features of the short-term geodetic deformation patterns in the western Transverse Ranges.

3. Geodetic Data

3.1. Continuous GPS Data

[8] Increases in the volume and availability of data from continuous GPS sites throughout the western Transverse Ranges provide the opportunity to better constrain the spatial patterns of surface deformation than in past works. Before using this geodetic data, we first must assess the quality of the available GPS data, which record the sum of all deformation signals, including tectonic deformation, seasonal deformation, and anthropogenic deformation. In this work, we analyze data from 52 continuous GPS stations from the Plate Boundary Observatory network in the region of interest. Time series data are derived from combined filtered solutions, which represent the combination of a GIPSY (https://gipsy-oasis.jpl.nasa.gov/) and GAMIT (http://www-gpsg.mit.edu/~simon/gtgk/) solution that has the common mode error from the entire network removed (following the methods described in *Dong et al*. [1998, 2006]). While network-wide filtering had already been performed on the filtered time series data, local nontectonic signals may still be present. For example, some continuous GPS data in the nearby Los Angeles Basin exhibit velocities that are contaminated by both seasonal and longer-term anthropogenic deformation due to groundwater extraction and hydrocarbon exploration [*Argus et al*., 2005; *Bawden et al*., 2001]. Whether the geodetic velocities in the western Transverse Ranges are contaminated and to what degree have not previously been determined. Since continuously recording GPS sites have sufficient temporal resolution to distinguish secular rates (potentially tectonic) from periodic (potentially seasonal and nontectonic) and irregular (potentially anthropogenic) deformation signals, we can apply several techniques to estimate both the tectonic and nontectonic components of deformation.

[9] Our time series analysis approach closely follows *Dong et al*. [2006], except that we do not implement the Karhunen-Loeve expansion for spatial filtering. Using the software package QOCA [*Dong et al*., 2006], we perform regional filtering by first simultaneously estimating and removing (1) bias terms, (2) time series offsets due to episodic events (coseismic offsets, orbital shifts, and/or equipment changes), (3) annual/semiannual periodic motion, and (4) secular velocities (Figure 2). Then, to determine which of the remaining nonlinear signals are spatially coherent and thus likely to be nontectonic in origin, we perform principal component analysis (PCA) on the residual data and remove the scaled first principal components (i.e., the common mode error) from each raw time series to form a regionally filtered data set.

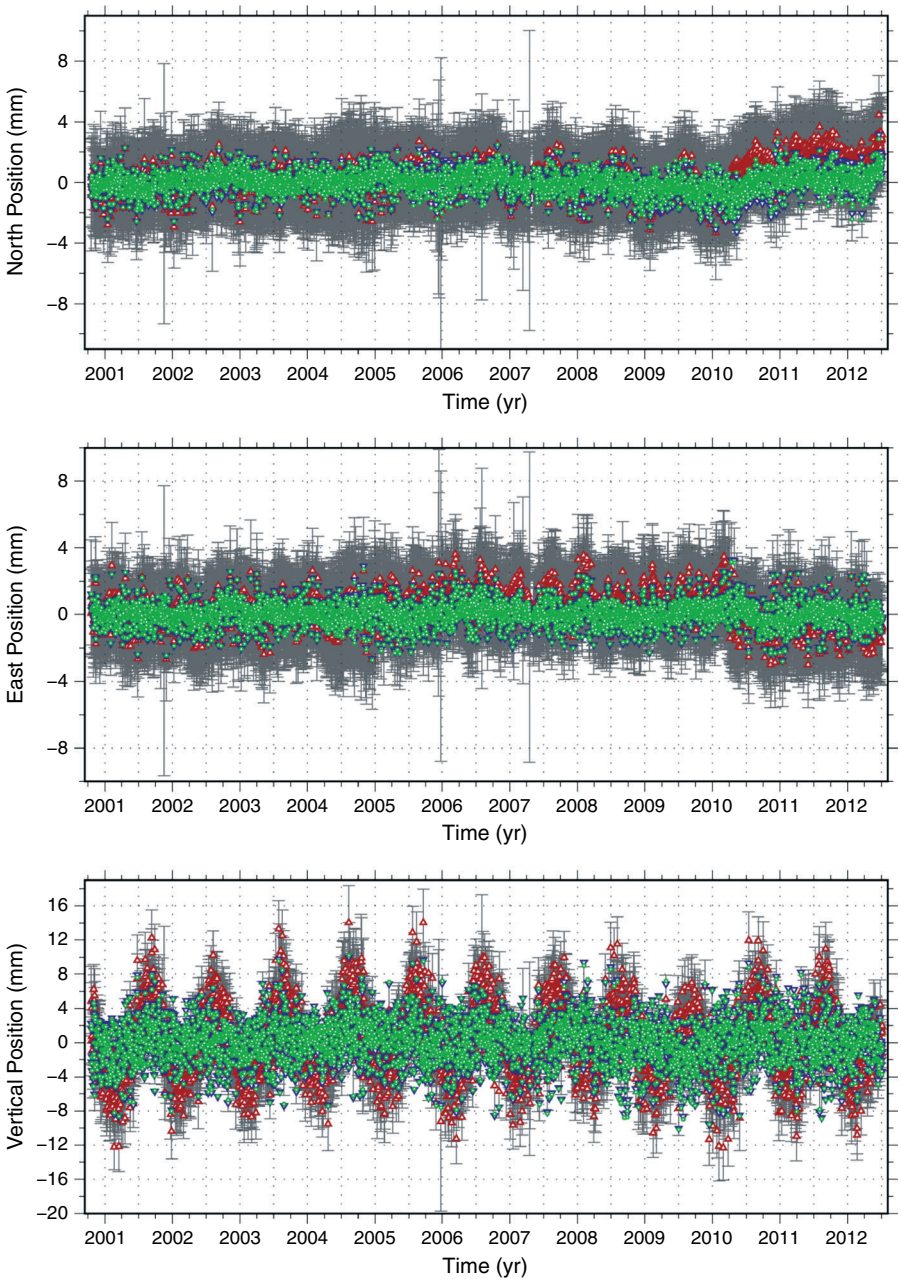

Figure 2. Example of GPS time series processing results for site CIRX. Each component of motion is detrended and is shown separately. Red triangles show the raw MEaSUREs combined filtered time series; blue inverted triangles show the time series after removal of bias, offsets (coseismic, orbital, and equipment changes); and the green circles show the final time series after removal of common mode error via principal component analysis [i.e., *Dong et al*., 2006]. Because the MEaSUREs-filtered time series already has the network-wide common mode errors removed, it is not surprising that the common mode filtering does not significantly alter most time series. The weighted RMS error (WRMS) for this site was reduced from 2.14 to 1.45 mm/yr, and the average WRMS for all sites was 2.67 mm/yr for the raw data and 1.86 mm/yr for the final processed time series data. In the end, the resultant time series are dominantly linear, suggesting successful removal of noninterseismic motions.

We then repeat the estimation of bias terms, episodic offsets, annual/semiannual motions, and secular velocities on the regionally filtered data. In the end, the time series are dominantly linear with a considerable reduction in root mean square (RMS) error, suggesting that the majority of temporally variable nontectonic signals have been removed (Figure 2).

[10] Formal errors on GPS velocities presented here are calculated using the standard white + flicker noise temporal model [*Dong et al*., 2006]. If our time series data has a significant random-walk or power law noise component, our formal error ranges could be too small by more than an order of magnitude [*Langbein*, 2012]. The question of which

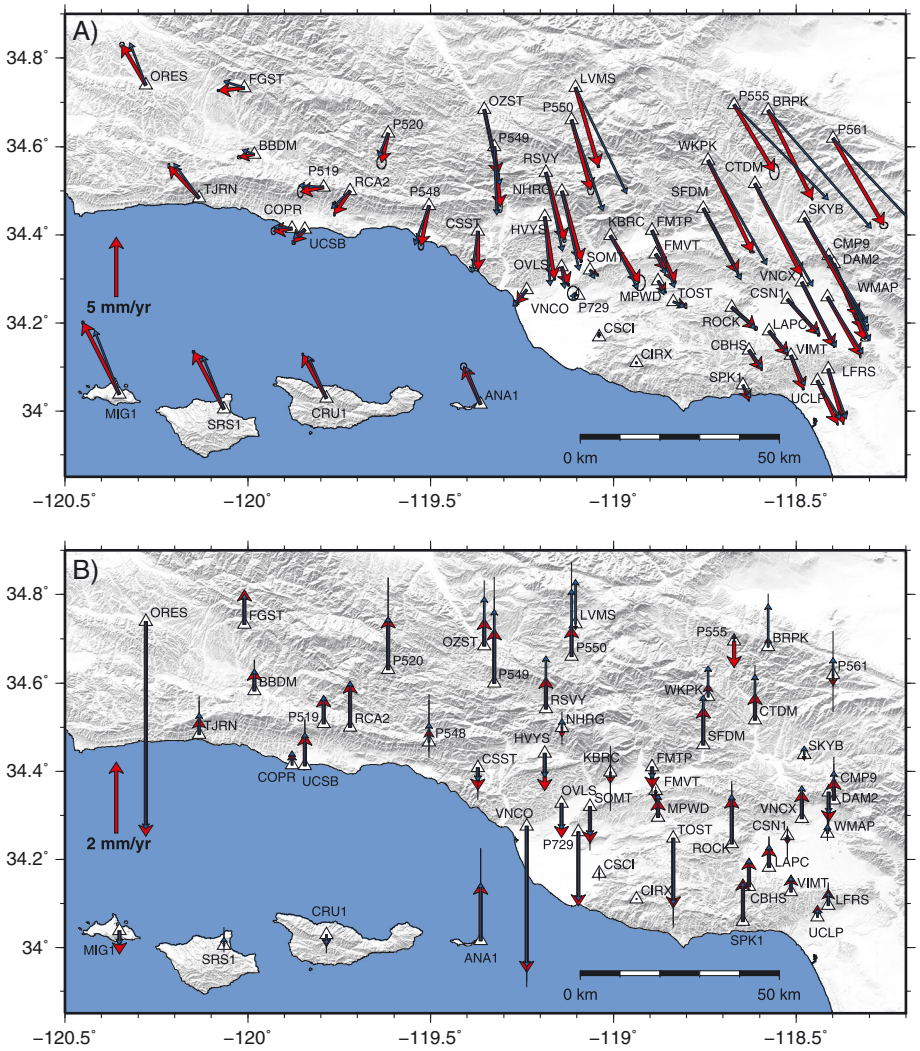

Figure 3. GPS velocities relative to site CIRX. Velocities before San Andreas strain removal are shown with the thinner blue arrows while the GPS velocities with strain due to the locked San Andreas fault removed are shown with red arrows. 95% confidence ranges are plotted, but because most time series are rather long (>10 years) and have continuous data, the formal errors are very small (typically <0.2 mm/yr). (a) Horizontal velocities. (b) Vertical velocities.

temporal model to use when estimating constant velocities from GPS time series is still a matter of much debate [e.g., *Langbein*, 2004, 2012]; therefore, determination of the temporal noise characteristics for our time series is beyond the scope of this work. Because of this, we caution the reader that our formal error estimates on GPS velocities are likely too small, and fitting model data within the formal errors is unlikely. We instead focus our efforts on minimizing the RMS residuals between models and the GPS data.

[11] While the raw time series data are all processed in the ITRF2005 reference frame, we present all GPS velocities here relative to site CIRX, located in the Santa Monica Mountains, to highlight local deformation patterns. To which site the GPS velocities are relatively plotted has no effect on the deformation (strain rate) patterns. We choose to plot velocities relative to site CIRX because it exhibits a very linear time series (Figure 2) and is geographically located at the south-central portion of our area of interest; therefore, any north/south contraction should be easy to visually identify in the regional network. The spatial pattern of the resultant GPS velocities clearly shows a component of right-lateral shear consistent with strain accumulation along the locked San Andreas fault, as well as contraction across the Ventura Basin (Figure 3). Because we are only interested here in the deformation due to the faults of the western Transverse Ranges, we remove the strain associated with the San Andreas fault using a simple rectangular dislocation model using the solutions of *Okada* [1985]. The dislocation model of the San Andreas fault uses parameters identical to that of *Argus et al*. [2005]; however, we do not remove strain associated with the San Jacinto fault because all of the GPS sites analyzed here are >100 km from its northern terminus, and any strains in the western Transverse Ranges associated with locking along it are negligible. In the end, the corrected GPS velocities (provided in the supporting information) and associated gradients dominantly reflect the local strain-inducing process within the western Transverse Ranges, including the following: (1) regional contraction due to the network

of oblique reverse faults [e.g., *Donnellan et al*., 1993a; *Hager et al*., 1999], (2) regional block rotation, likely due to the much longer, plate-bounding faults [e.g., *Becker et al*., 2005; *McCaffrey*, 2005; *Meade and Hager*, 2005], (3) off-fault strain accumulation due to active folding and sedimentary basin deformation [e.g., *Azor et al*., 2002; *Hager et al*., 1999; *Hubbard et al*., submitted to *Bulletin of the Seismological Society of America*, 2013; *Yeats*, 1977; *Yeats et al*., 1988], and (4) the effects of localized anthropogenic activity such as groundwater extraction/recharge and hydrocarbon pumping [e.g., *Argus et al*., 2005; *Bawden et al*., 2001].

3.2. Persistent-Scatterer InSAR Data

[12] The presence of a linear time series in GPS data implies steady state motion but does not guarantee that the motion is tectonic in origin. Several GPS stations in the nearby Los Angeles Basin are currently undergoing subsidence from long-term aquifer draw-down [*Argus et al*., 2005; *Bawden et al*., 2001], introducing a long-term trend in the time series. Dense geodetic data, such as what InSAR provides, allow identification of localized spatial anomalies in the velocity field [*Bawden et al*., 2001]. The spatial resolution of the GPS data used here is too coarse (typically $>$10 km spacing) to identify such features. Therefore, we supplement the GPS data with a complementary and spatially dense InSAR data set to determine if any GPS sites are likely to be contaminated by anthropogenic deformations.

[13] Because a significant portion of the western Transverse Ranges is vegetated and/or contains steep topographic slopes, backscattered radiation from radar satellites imaging the region may become severely decorrelated over time [*Hooper et al*., 2004; *Zebker and Villasenor*, 1992], rendering traditional "2-pass" InSAR methods ineffective. These problems may be mitigated to a large degree by applying an advanced processing methodology to the full archive of satellite radar data for the region to identify "persistent scatterers" (PS)—targets on the ground that, when imaged, provide radar returns that are stable throughout time. Several methods, including the Permanent Scatterer InSAR (PSInSAR) technique [*Ferretti et al*., 2001] as well as the Stanford Method for Persistent Scatterers (StaMPS) technique of *Hooper et al*. [2004] have been demonstrated to increase both the precision of surface range-change velocity estimates and the spatial density of observation points over traditional InSAR methods, particularly in challenging (e.g., vegetated) terrains [e.g., *Ferretti et al*., 2001; *Hooper*, 2008; *Hooper et al*., 2007; *Hooper et al*., 2004]. The different PS methods differ in the assumptions used to unwrap the phase of the radar interferograms that they produce. The method of *Ferretti et al*. [2001] assumes a functional form for the deformation signal, whereas the StaMPS method of *Hooper et al*. [2004] uses the spatial pattern of phase in the unwrapping process. The advantage of the latter method, for our purposes, is that it requires no a priori knowledge of the expected patterns of deformation with time. The resulting data set gives a displacement time series, for each PS, from which one can calculate a best-fitting velocity.

[14] We apply the StaMPS approach of *Hooper et al*. [2007] to a 23-image data set acquired by the Envisat satellite (track 213, frames 2907–2925) spanning the period 2005–2010. The InSAR data overlap in time with the continuous GPS data and are therefore appropriate to use in detection of nontectonic motions in the GPS data. While some PS algorithms require $>$25 images, the StaMPS algorithms are typically successful even with only 12 images and sometimes as few as four images [*Hooper et al*., 2007]. Thus, the 23 available images should be sufficient to detect centimeter- to millimeter-scale ground motions. We generate interferograms using a combination of the DORIS (http://doris.tudelft.nl/) and ROI_PAC (http://www.roipac.org/) software packages following the typical StaMPS workflow. The digital elevation model is derived from the Shuttle Radar Topography Mission (STRM) 1 arcsecond data. A plot of the perpendicular baselines for the selected scenes is included in the supporting information. The resultant full-resolution persistent-scatterer data set presented here contains more than 10^6 data points (Figure 4).

[15] Our processed persistent-scatterer InSAR data show a strong increase in line of sight (LOS) velocity from south to north, consistent with interseismic deformation due to the locked San Andreas fault (see supporting information). For our purposes here, we only seek to use the InSAR to locate localized zones of deformation not related to tectonics [e.g., *Argus et al*., 2005; *Bawden et al*., 2001], so after determining the persistent scatterers, we estimated and removed the best-fitting long-wavelength orbital ramp for each interferogram. By removing the ramps, we have likely removed a significant portion of the long-wavelength interseismic deformation due to the San Andreas and possibly some of the contraction throughout the Transverse Ranges. The removal of any long-wavelength deformation, whether due to orbital geometry fluctuations or tectonics, is advantageous for our purposes because the spatial patterns of InSAR LOS velocities are effectively detrended and localized anthropogenic deformation will be easier to identify visually. In total, we identify six locations of anthropogenic or nontectonic motions (Figure 4a); however, only two locations are near enough to any GPS sites to warrant further discussion (Figure 4b).

[16] The first of these possible anthropogenic signals is located in the greater Oxnard area (location "D" in Figure 4), an area of range-change rate increase consistent with subsidence of the ground. GPS site P729 lies on the edge of this zone of inferred subsidence (Figure 4b), likely resulting in an increased westward component of motion at that site [*Bawden et al*., 2001]. We also identify a small and localized zone of range-change-rate increase northwest of site VNCO, near the Ventura Avenue anticline where ongoing hydrocarbon production is occurring (location "C' in Figure 4). Since this zone of inferred subsidence is highly localized, the nearby GPS site, VNCO, is not affected (Figure 4b). We note that the GPS data for site VNCO does have an anomalously fast subsidence rate compared to nearby GPS sites suggesting the potential for a highly localized vertical anthropogenic deformation source; however, a clear anthropogenic signal is not clear in the InSAR data (Figure 4b). Thus, based on the InSAR data, GPS site P729 may have anthropogenic contamination, but the remaining GPS sites should provide reliable tectonic velocities. The relative lack of anthropogenic deformation is in stark contrast to

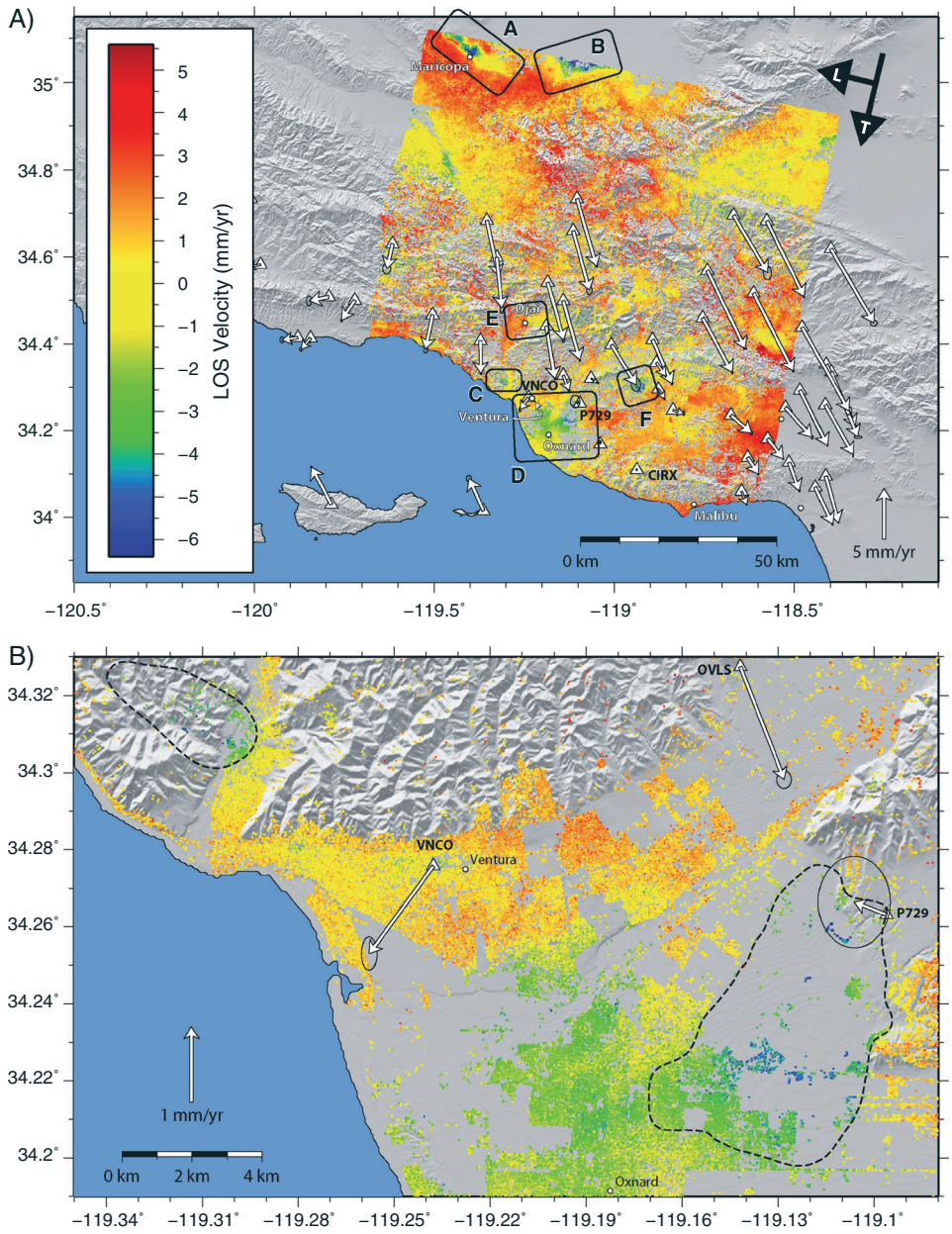

Figure 4. Average LOS velocities for the western Transverse Ranges region derived from the persistent-scatterer analysis of Envisat data. Black arrows indicate the along-track (T) and look (L) directions. All motions are relative to the LOS data at the location of GPS site CIRX. Cities are labeled with white circles and text. Six rectangles highlight zones of localized subsidence, which are likely anthropogenic in nature. Zone A: Subsidence due to hydrocarbon extraction near Maricopa. Zone B: Subsidence likely due to a combination of hydrocarbon extraction, groundwater removal from a combination of agricultural uses and a nearby sand and gravel quarry. Zone C: Highly localized subsidence due to hydrocarbon extraction along the Ventura Avenue anticline. Zone D: Subsidence likely due to groundwater extraction for metropolitan uses in the Ventura/Oxnard region. Zone E: Localized subsidence to due groundwater extraction for agricultural and domestic uses near Ojai. Zone F: Localized subsidence due to unknown causes. Zone F contains nothing that can be clearly attributed to the localized subsidence. Since no GPS sites are in this zone, we do not attempt to discern the cause of this anomalous motion. (b) Zoomed in view of the InSAR data for the Ventura/Oxnard region. The two dashed zones show subsidence due to hydrocarbon extraction along the Ventura Avenue anticline (top left) and anthropogenic subsidence near site P729 (bottom right zone). While GPS station VNCO may have an anomalously fast vertical velocity, we cannot confidently identify any significant anthropogenic motions within the noise level (~1–2 mm/yr, depending on location) of the InSAR data. In the end, while several zones of anothropogenic motion have been identified, only GPS site P729 is located near the edge of a subsiding zone, where significant nontectonic horizontal motions are expected [e.g., *Bawden et al*. 2001], likely resulting in a contaminated an unreliable velocity.

the nearby Los Angeles Basin, where anthropogenic motions due to groundwater extraction are found in many locations and may significantly contaminate a large number of GPS velocities [*Argus et al*., 2005; *Bawden et al*., 2001]. Given the significantly lower population density of the western Transverse Ranges compared to the Los Angeles Basin, the relative lack of significant nontectonic motions is perhaps not surprising.

4. Geodetic Estimates of Strain Rates

4.1. Strain Inversion Methodology

[17] During the interseismic period, active faults are expected to produce strain localizations above their creeping upper tip lines [e.g., *Savage*, 1983; *Savage and Burford*, 1970, 1973]; therefore, mapping out the distribution of strain in a region can be useful for identifying active faults and characterizing deformation patterns throughout a region [e.g., *Allmendinger et al*., 2007; *Allmendinger et al*., 2009; *Donnellan et al*., 1993b; *Shen et al*., 1996; *Titus et al*., 2011]. Using the corrected horizontal GPS velocities, we can estimate the horizontal velocity gradient tensors e_{ij}, which can then be decomposed into infinitesimal strain rate tensors, ε_{ij}, and rotation rate (vorticity) tensors, ω_{ij}, using

$$e_{ij} = \varepsilon_{ij} + \omega_{ij} = \left(\frac{e_{ij} + e_{ji}}{2}\right) + \left(\frac{e_{ij} - e_{ji}}{2}\right). \quad (1)$$

Useful aspects of the strain rate tensors can be directly calculated including the principal contraction rates (eigenvalues of ε_{ij}) and principal strain directions (eigenvectors of ε_{ij}).

[18] Calculating the velocity gradient tensor from velocity and spatial information associated with the GPS sites can be formulated as a linear inverse problem that can be solved using several standard methods that are discussed in detail by *Allmendinger et al*. [2007] and *Shen et al*. [1996]. In general, because there are six unknowns in two dimensions (two translation terms and four components of the velocity gradient tensor), the simplest inversion requires the GPS network to be triangulated, and a uniform strain rate tensor can be calculated for each triangle [*Allmendinger et al*., 2007]. This method yields unreliable results for our geodetic network because the station location geometry is unevenly spaced, resulting in several highly elongated triangles that yield poor estimates of strain. Therefore, in order to provide a more robust estimate of regional strains, we use more than three GPS sites and utilize two standard least squares inversion methods to solve the overconstrained problem.

[19] The first inversion method involves performing a gridded nearest-neighbor interpolation of the GPS data and using the standard solution for a least squares inversion [*Menke*, 1989]:

$$\mathbf{m} = \left[\mathbf{G}^{\mathbf{T}}\mathbf{G}\right]^{-1}\mathbf{G}^{\mathbf{T}}\mathbf{d}, \quad (2)$$

where **G** is the design matrix containing the GPS position vectors of each grid point, **d** is a column vector containing the GPS velocities, and **m** is a column vector that contains the two translation terms and the four velocity gradient tensor components. The exact compositions of **G**, **d**, and **m** are given by *Allmendinger et al*. [2007].

[20] The second method involves using the entire GPS velocity data set at each grid node and weighting each station's velocity by its distance from the node using

$$W = \exp\left(\frac{-d^2}{2\alpha^2}\right), \quad (3)$$

where d is the distance between the grid point and each station and α is a distance decay constant that describes how each station's effect decays with distance [*Shen et al*., 1996]. W is formed into a diagonal matrix and incorporated into the standard weighted least squares solution [*Menke*, 1989] as

$$\mathbf{m} = \left[\mathbf{G}^{\mathbf{T}}\mathbf{W}\mathbf{G}\right]^{-1}\mathbf{G}^{\mathbf{T}}\mathbf{W}\mathbf{d}. \quad (4)$$

This form of distance weighting results in Gaussian smoothing of the resultant strain rate field.

[21] Both inversions are performed on a regular grid with 3 km spacing. The nearest-neighbor inversions presented here use velocity data for the four nearest neighbors within 40 km of each grid point, and the distance-weighted inversions use all GPS sites weighted by a distance decay constant $\alpha = 10$ km. We choose a value of α that is similar to the station spacing [e.g., *Allmendinger et al*., 2009], resulting in zones of fast convergence in both inversions covering roughly the same area. Larger values of the distance decay constant effectively smear out and obfuscate local variations in strain. Examples of less smoothed and oversmoothed inversions are provided in the supporting information. In the end, neither strain inversion method is without inherent and unavoidable flaws. For example, there is no rigorous way to enforce strain compatibility in such an inversion [2007; *Allmendinger et al*., 2009]. The distance-weighted method is advantageous because it uses the entire data set at each grid point and calculates the strains as a continuous function in space; however, the drawback is that the degree of smoothing is controlled by the distance decay constant, which effectively smears out localized variations in strain. The nearest-neighbor method requires no assumptions about smoothing but is highly sensitive to small errors in the GPS velocities when stations are densely spaced. In the end, the nearest-neighbor inversions will likely produce a less smooth solution compared to the distance-weighted inversions, possibly overestimating strain rates in some locations with closely spaced data.

[22] We perform both inversions on the GPS data but caution the reader that neither inversion is without inherent mathematical and mechanical limitations; therefore, our focus here is on describing general regional-scale patterns and trends and not matching specific strain magnitudes or highly localized anomalies present in the inversion results.

4.2. Spatial Variations in Strain Rates

[23] Since the faults of the western Transverse Ranges are hypothesized to be dominantly reverse slipping [*Donnellan et al*., 1993a; *Hager et al*., 1999; *Huftile and Yeats*, 1994, 1995], variations in contraction across the region are of primary interest. Both nearest-neighbor and distance-weighted inversions of the horizontal GPS velocities show a band of relatively fast contraction localized near the central Ventura Basin (surrounding the San Cayetano and Oak Ridge faults),

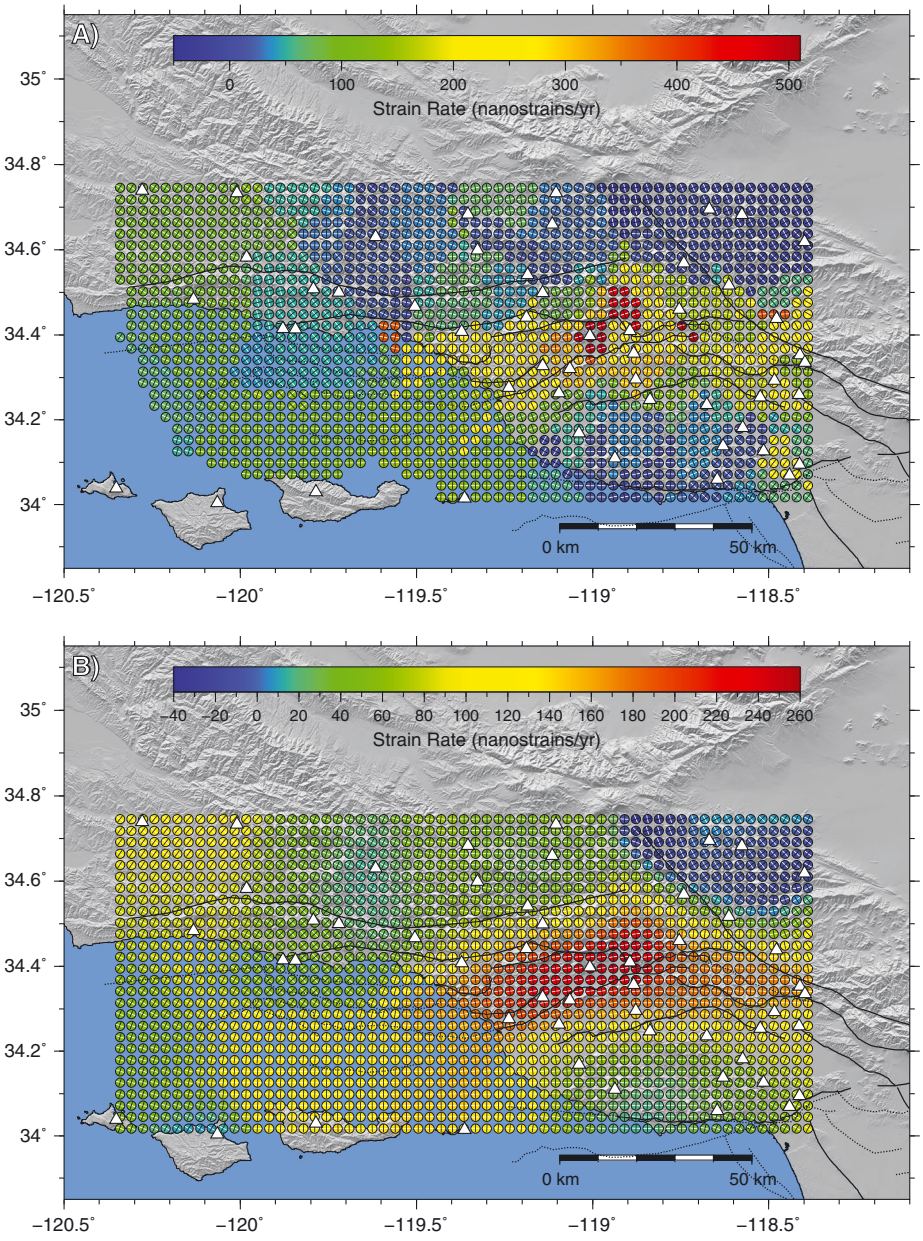

Figure 5. Maximum principal contraction rates and directions throughout the western Transverse Ranges calculated from inversions of the corrected horizontal GPS velocities. Fault traces follow from Figure 1, and GPS site locations are plotted as white triangles. Refer to Figure 2 for station names. Black tick marks show the direction of maximum principal contraction while white tick marks show the directions of maximum principal extension. (a) A nearest-neighbor interpolation and a least squares inversion. (b) A distance-weighted inversion. Both inversions highlight that fast contraction rates are localized near the central Ventura Basin, generally follow the trend of the basin, and decrease to the west and east.

with contraction rates decreasing both to the east and to the west (Figure 5). Assuming that locking depths through this relatively small region are approximately uniform [e.g., *Donnellan et al*., 1993a; *Hager et al*., 1999], this zone of localized fast contraction implies that the fastest fault slip rates are likely to occur on faults near the central Ventura Basin, with slip rates decreasing both to the east and to the west, or significant changes in rock stiffness exist throughout the region. Beyond the coastline to the west, the inversions show decreases in contraction rates; however, the lack of GPS data within the Santa Barbara channel prevents accurate detection of any potential zones of localized fast contraction. Thus, whether this localized zone of fast contraction continues offshore is not constrained given the available GPS data.

[24] Both inversions also produce a zone near the San Andreas fault in the northeast corner of the data, where both horizontal principal strains are very small or even extensional. Because the three northeasternmost sites are most sensitive to the details of the dislocation model used to remove San Andreas strain from the GPS data, we expect the calculated strain rates to be slow. Therefore, the zone of extension is likely due to simplifications in the dislocation

model used to correct the GPS data and is probably not real. Thus, the three northeasternmost GPS sites appear to have the vast majority of San Andreas fault strain effects removed; however, we concede that due to the simplistic nature of the San Andreas dislocation model used to correct the GPS data, these sites likely provide less reliable estimates of local deformation.

4.3. Estimates of Regional Strain and Rotation Rates

[25] An additional calculation that can be made from the geodetic data is an estimate of the average regional strain rate along with a regional vertical axis rotation rate. Such estimates have been used for determining appropriate tectonic boundary conditions in mechanical models [e.g., *Cooke and Marshall*, 2006; *Griffith and Cooke*, 2005; *Marshall et al*., 2008, 2009] as well as estimating the amount of off-fault deformation in a region [e.g., *McCaffrey*, 2005; *Titus et al*., 2011]. To calculate a best-fitting regional strain and rotation rate, a least squares inversion can be made of the entire horizontal GPS velocity data set using equation (2) [*Allmendinger et al*., 2012], excluding any sites that are deemed to be unreliable. We exclude sites P561, BRPK, and P555 because they are nearest to the San Andreas fault and are therefore most sensitive to the details of the dislocation model used to correct the GPS data. We also exclude site P729 because its velocity is likely contaminated by anthropogenic motions (Figure 4). The whole network inversion results in a best-fitting principal contraction rate of 101 ± 8 nanostrains/yr oriented at N5°E ± 1°, with a principal extension rate of 36 ± 2 nanostrains/yr oriented perpendicular to the contraction direction. The error ranges are determined by performing a jackknife test on the regional data. Using a significantly smaller GPS data set of 15 sites, *Marshall et al*. [2008] estimated a regional principal contraction rate of 121 nanostrains/yr oriented at N9°W and an identical principal extension rate of 36 nanostrains/yr.

[26] We estimate a regional vertical axis rotation rate of 2.3 ± 0.1°/Myr in a clockwise direction, which is in agreement with the direction of rotation inferred from several past studies but generally slightly slower than most estimates of rotation throughout the western Transverse Ranges [e.g., *Donnellan et al*., 1993b; *Jackson and Molnar*, 1990; *Lamb*, 1994; *Luyendyk*, 1991; *Luyendyk et al*., 1980]. For example, using kinematic models of rotation, *Lamb* [1994] estimates 2.4–3.5°/Myr of clockwise rotation, although the rates are predicted to be rather temporally variable. Using very long baseline interferometry data, *Jackson and Molnar* [1990] estimate 3–9°/Myr, and *Donnellan et al*. [1993b] use GPS and triangulation data to estimate 4–7°/Myr clockwise, with localized regions rotating up to 10°/Myr. *McCaffrey* [2005] estimates a negligible amount of rotation of the "VENT" block (the western Transverse Ranges block), but this estimate is based on inverting residual GPS velocities after the effects of a block model have been removed, so the significantly slower rate of *McCaffrey* [2005] is not unexpected.

5. Three-Dimensional Mechanical Models of Faulting

[27] In order to better characterize current fault slip rates and distributions in the western Transverse Ranges of southern California, and to test whether these slip rates are consistent with both geologic and interseismic geodetic data, we update the results of *Marshall et al*. [2008] with our improved geodetic data and an updated fault model. We achieve this using an established mechanical modeling methodology ideal for simulating both long-term geologic timescale deformation and short-term interseismic deformation in a network of complex, interacting, nonplanar, and finite faults [i.e., *Marshall et al*., 2009]. To build and improve on the method of *Marshall et al*. [2009], we have provided a quantitative assessment of the regional strain rate, including reasonable error ranges (see section 4), and we also compare model strain rate patterns to those inverted from GPS data to further evaluate the model fit to data.

5.1. Modeled Fault Surface Geometry

[28] In this work, we create and use a three-dimensional tessellated triangular fault mesh based on the Southern California Earthquake Center Community Fault Model (CFM) version 4.0. The CFM representation [*Plesch et al*., 2007] of the western Transverse Ranges region contains numerous discontinuous three-dimensional fault surfaces constrained by all available geologic and geophysical data, many of which exhibit considerable deviations from planarity. Because the CFM contains a highly irregular triangulated mesh, we have remeshed all of the fault surfaces to attain a relatively uniform element size while honoring the details of the CFM geometry. In all, the modified CFM mesh contains 7403 triangular elements that form 44 faults throughout the Transverse Ranges region (Figure 1). The average element length is approximately 3.5 km, with an approximate average surface area of 6.1 km^2. Element size varies throughout the model, with generally smaller elements near the surface. While we focus on the western Transverse Ranges region, we include faults in the Santa Barbara Channel and many faults in the Los Angeles Basin to the east in order to capture any mechanical interactions between these nearby fault systems. Therefore, the fault mesh used here is essentially an improved version of the CFM 2.5 mesh used by *Marshall et al*. [2008] and merged with many of the Los Angeles faults from *Marshall et al*. [2009], with all fault surfaces updated to honor the CFM 4.0 geometries. A three-dimensional interactive version of our fault mesh is provided with the accompanying supporting information.

5.2. Mechanical Model Setup

[29] Because the distribution of slip on complex nonplanar fault surfaces cannot be known a priori [e.g., *Dieterich and Smith*, 2009; *Griffith et al*., 2010; *Kaven et al*., 2011; *Marshall and Morris*, 2012; *Marshall et al*., 2008; *Ritz and Pollard*, 2012], we use the numerical Boundary Element Method (BEM) computer program, Poly3D [*Thomas*, 1993], to determine the distribution of slip on faults and deformation patterns throughout the western Transverse Ranges region. The advantage of Poly3D is that it can be used to calculate both kinematically and mechanically valid nonuniform slip distributions on arbitrarily shaped three-dimensional fault surfaces, while simultaneously accounting for mechanical interactions between all modeled fault elements. In comparison, the block modeling technique satisfies only kinematic compatibility through a path integral constraint [*McCaffrey*, 2005; *Meade and Hager*, 2005]. Thus, the calculated slip distributions in a block model are

kinematically compatible with the GPS data, but not necessarily mechanically feasible. Poly3D is well suited and has been widely used for the task of determining the distribution of slip on the complex network of faults throughout southern California [e.g., *Cooke and Marshall*, 2006; *Dair and Cooke*, 2009; *Griffith and Cooke*, 2004, 2005; *Herbert and Cooke*, 2012; *Marshall et al*., 2008, 2009; *Meigs et al*., 2008].

[30] We create interseismic models in a two-step process that follows the approach of *Marshall et al*. [2009], but for clarity, we describe the setup and boundary conditions of each model below.

5.2.1. Modeling Geologic Timescale Deformation

[31] First, we create a geologic timescale model simulating 5000 years of deformation, where deformation is driven from below by applying slip along a basal horizontal crack. Since frictionless elastic models are not time dependent and we seek to find the time-averaged behavior, the exact choice of how many years are modeled is unimportant. The Los Angeles Regional Seismic Experiment seismic data reveal that reverse faults throughout the Transverse Ranges region are truncated by a subhorizontal, midcrustal décollement [*Fuis et al*., 2001, 2003]. Past models of the Transverse Ranges best fit geodetic data when strike-slip faults were modeled as semi-infinite (in vertical height), and reverse faults merged into horizontal structures at depth [e.g., *Marshall et al*., 2009; *Shen et al*., 1996]. The basal horizontal crack used in our models provides two benefits. First, the horizontal crack mechanically unpins the lower tip lines of strike-slip faults, simulating semi-infinite height (see *Marshall et al*. [2009] for detailed solution). Second, the deep horizontal crack reproduces the truncated reverse fault structure observed in seismic imagery [e.g., *Fuis et al*., 2001, 2003] and allows reverse faults to slip horizontally at depth, as suggested by *Shen et al*. [1996]. While the depth to the horizontal basal crack has no effect on strike-slip rates, dip-slip rates will increase with increasing depth to the horizontal crack [*Marshall et al*., 2009]. Thus, a shallower basal crack would produce slower reverse slip rates and result in more diffuse interseismic surface deformation. In the end, this model configuration reproduces the basic crustal fault structure of the Transverse Ranges region and provides an efficient way to simulate lower crustal deformation within a region containing numerous nonparallel and finite active faults. We note that this particular geometric configuration may not be applicable to all regions of convergent active faulting.

[32] In all models presented here, we place the basal crack at 27.5 km depth, the approximate depth of the Moho in the region [*Fuis et al*., 2001; *Magistrale et al*., 2000]. The compositional and stiffness contrast between the crust and mantle may facilitate development of a décollement. Although the depth of the horizontal crack has no effect on strike-slip fault slip rates, we choose a depth greater than 20 km for the crack because moderately dipping reverse faults have been observed to slip below 20 km depth during the 1994 Northridge earthquake [e.g., *Carena and Suppe*, 2002; *Hudnut et al*., 1996; *Wald et al*., 1996]. Based on results from existing mechanical models using a similar deep horizontal crack [*Cooke and Marshall*, 2006; *Cooke and Dair*, 2011; *Dair and Cooke*, 2009; *Herbert and Cooke*, 2012; *Marshall et al*., 2008, 2009; *Meigs et al*., 2008], we expect the model predicted surface deformation to be relatively insensitive to our choice of 27.5 km depth for the horizontal crack.

[33] In the geologic timescale model, we drive deformation from below [e.g., *Fay and Humphreys*, 2005; *Jolivet et al*., 2008] by applying slip along the periphery of the basal horizontal crack until the modeled region deforms at the average regional strain rate determined from the GPS inversions (see section 4.3). We then insert the CFM-based faults and apply a shear stress free (i.e., frictionless) boundary condition for all modeled fault elements. This allows faults to freely interact and accumulate mechanically viable and spatially variable slip distributions at all depth levels in response to the applied regional contraction. Slip rates from the geologic timescale model can be directly compared to geologic estimates of fault slip rates [e.g., *Marshall et al*., 2009]. In the end, the overarching purpose of the geologic timescale model is to test whether the current day regional strain rates are mechanically compatible with the long-term geologic slip rates.

5.2.2. Modeling Interseismic Timescale Deformation

[34] In the second step of our mechanical modeling methodology, we simulate interseismic deformation by applying the slip distribution from the geologic timescale model to only fault elements below a user-specified locking depth. This process is mathematically identical to the back slip approach of *Savage* [1983], which is also utilized by most block models [*Becker et al*., 2005; *McCaffrey*, 2005; *Meade and Hager*, 2005]. Because the interseismic timescale models have the distribution of slip applied, Poly3D can calculate the surface velocities or strain rate patterns analytically. The regional strain rate estimates suggest a significant component of block-like rotation. To allow direct comparison with the GPS and strain rate data, we add the regional rotation rate to the interseismic model results. In the end, the interseismic models allow us to test whether the mechanically viable slip distribution from the complex network of faults in the geologic model can also reproduce the currently measured interseismic geodetic velocities and strain rate patterns throughout the region.

5.3. Long-Term Fault Slip Rate Results

[35] In order to determine if the contemporary regional strain rates inferred from GPS are compatible with long-term slip rates estimated from geology, we compare results from the geologic model to existing geologic slip rate estimates (Figure 6). The models presented here predict spatially variable slip rates that vary as a function of each fault element's orientation, surface area, and distance from fault tips, the free surface, and other fault elements. We calculate area-weighted average slip rates for each modeled fault that can be considered reasonable estimates for each fault's average slip behavior [*Cooke and Marshall*, 2006; *Marshall et al*., 2008, 2009]. To quantify the variation in slip behavior across each fault surface, we calculate the 1σ range for each fault surface and report these as error bars (Figure 6).

[36] The model prediction of slip rates on the Holser and Simi faults are faster than existing geologic estimates. The Holser fault slip rate is based on a measured offset of the Saugus Formation and is poorly constrained [*Peterson et al*., 1996]. The Simi fault slip rate estimate is based on a paleoseismic study very near the fault tip [*Gonzalez and Rockwell*, 1991], a location that is expected to and has been shown to produce anomalously slow slip [see *Marshall et al*., 2008]. Therefore the apparent slip rate mismatch at these two faults is most likely due to nonrepresentative or

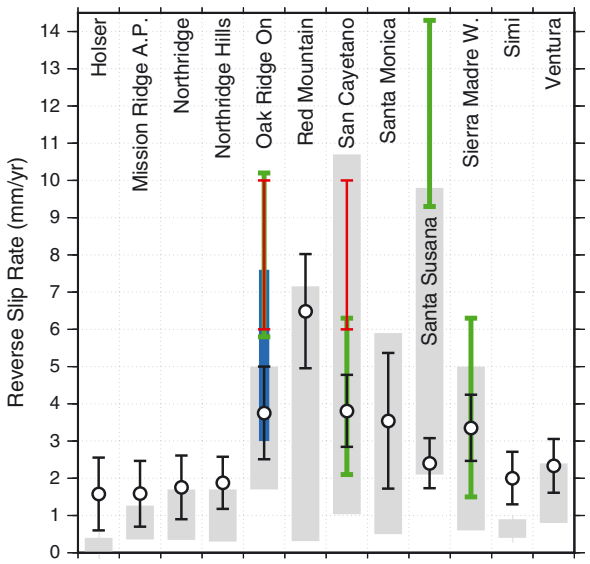

Figure 6. Comparison of model-calculated average slip rates (black circles) to geologic (gray rectangles) block model (green: *Meade and Hager* [2005]; blue: *Loveless and Meade* [2011]), and two-dimensional models (red: *Donnellan et al.* [1993a] and *Hager et al.* [1999]) slip rate estimates. Because modeled fault surfaces have spatially variable slip rates, error bars on the model calculated slip rates show the 1σ range in slip across the entire fault surface. For geologic slip rate estimate ranges, refer to Table 2. Note that some outlier model-based predictions are not plotted. For example, block model predictions for the Santa Monica fault suggest a reverse slip rate of -5.7 ± 2.6 mm/yr [*Loveless and Meade*, 2011] and -0.2 ± 2.2 mm/yr [*Meade and Hager*, 2005], implying that the Santa Monica fault is a normal fault. Normal slip is inconsistent with abundant geologic evidence [*Dolan and Pratt*, 1997; *Dolan et al.* 2000; *Huftile and Yeats*, 1996] for reverse slip. Likewise, *Loveless and Meade* [2011] also predict a reverse slip rate of -2.4 ± 1.4 mm/yr on the Santa Ynez fault, although geologic constraints on this fault are poor [*Huftile and Yeats* 1995]. Lastly, while the models of *Hager et al.* [1999] match geodetic data very well, these models suggest an anomalously fast 7.8 ± 1.6 mm/yr of slip on both the San Cayetano and Oak Ridge faults (range depends on relaxation time). Slip rate predictions from *Becker et al.* [2005] and *McCaffrey* [2005] are not shown here because these models simplified the western Transverse Ranges into a single fault; thus, a comparison is not meaningful. In the end, the models presented here provide an improved fit with the geologic slip rate ranges compared to previous block and two-dimensional models.

inaccurate slip rate estimates and is not of significant concern. We note that the model predicted average slip rate on the Santa Monica fault falls within the total geologic range, but the model average slip rate estimate does not agree with the well-constrained 0.5 mm/yr slip rate estimate of *Dolan and Pratt* [1997]. The model estimate does fall within the 3.8–5.9 mm/yr estimate of *Davis and Namson* [1994]. The balanced cross sections of *Davis and Namson* [1994] focus on the deeper portions of the fault and the southern strand, while the *Dolan and Pratt* [1997] analysis focused on the northern echelon segmented strands. The model predicts spatially variable slip across the Santa Monica fault with generally faster slip on the deep and southern strand, with significantly slower slip on the echelon segmented northern strands (for the three-dimensional fault geometry, refer to the provided supporting information). Therefore, the model is consistent with both the *Dolan and Pratt* [1997] and the *Davis and Namson* [1994] estimates. The remainder of the model-predicted average slip rates all fall within the existing geologic slip ranges, suggesting that the current day strain rates measured by geodesy are compatible with long-term fault slip rates. Because the mechanical model fits existing geologic slip rate estimates well, the model is likely to provide reasonable estimates for the remaining faults throughout the western Transverse Ranges region, many of which are otherwise unconstrained (Table 2).

5.4. Interseismic Surface Velocity Results

[37] While the three-dimensional mechanical model predictions generally agree well with geologic slip rate estimates, we now determine if these slip rate distributions can reproduce the current geodetic velocities and strain rates. Because we do not directly invert for locking depth, we must forward model a range of locking depths and determine which best fits the geodetic data. Given an average fault element length of 3.5 km and that the fault mesh is irregular and does not allow for exactly constant locking depths, we expect that our models will only provide constraint on the locking depth at the few kilometers level. Because several sites were earlier deemed less reliable (P729, P555, BRPK, and P561) and there are large systematic residuals at several distal sites (ORES, TJRN, FGST, UCLP, LFRS, and VIMT), we exclude these sites from the preferred locking depth misfit analysis. Calculations from a suite of uniform locking depths reveal a best-fitting locking depth of 13 km (Figure 7). Including all of the reliable GPS data in the RMS error calculations reveals a best-fitting locking depth of 16 km (Figure 7). When all GPS sites are used in the RMS

Table 2. Geologic Slip Rates (mm/yr) From the 3D Mechanical Model

Fault Name	Net Slip	1σ	Reverse Slip	1σ	Strike Slip	1σ
Anacapa Dume	5.1	2.7	5.0	2.1	−1.0	1.7
Del Valle	0.4	0.3	0.3	0.2	0.3	0.3
Holser	1.6	1.0	1.6	1.0	−0.1	0.3
Malibu Coast	3.5	1.0	3.5	0.9	0.5	0.4
Mission Ridge/Arroyo Parida	1.6	1.0	1.6	0.9	−0.1	0.5
North Channel	0.6	0.3	0.6	0.2	0.1	0.1
Northridge	1.8	1.1	1.8	0.9	0.5	0.7
Northridge Hills	1.9	0.8	1.9	0.7	0.3	0.4
Oak Ridge Offshore	3.3	1.5	3.3	1.4	−0.3	0.4
Oak Ridge Onshore	4.5	1.5	3.8	1.2	−2.5	0.9
Pitas Point Montalvo	0.5	0.8	0.5	0.7	0.0	0.4
Red Mountain	6.5	1.7	6.5	1.5	−0.2	0.8
San Cayetano	3.8	1.3	3.8	1.0	0.3	0.8
San Gabriel North	6.2	1.7	2.2	1.2	5.8	1.2
San Gabriel South	4.2	1.8	3.5	0.7	2.3	1.7
Santa Monica	3.8	2.0	3.5	1.8	−1.5	0.7
Santa Susana	2.5	1.2	2.4	0.7	0.7	0.9
Santa Ynez	2.0	1.3	2.0	0.8	−0.3	1.0
Sierra Madre West	3.8	1.1	3.4	0.9	1.8	0.6
Simi	2.2	0.9	2.0	0.7	−0.8	0.5
Sisar	0.6	0.7	0.6	0.7	0.0	0.3
Ventura	2.6	1.1	2.3	0.7	−1.2	0.8
Verdugo	1.0	0.3	0.7	0.2	0.7	0.2

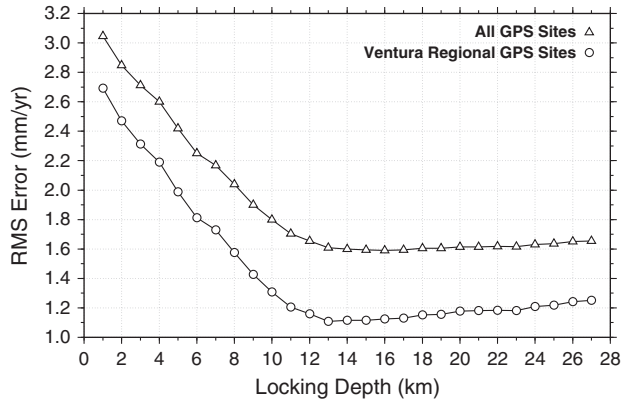

Figure 7. Plot of model fit to GPS (RMS error) for a range of locking depths. A 13 km locking depth minimizes misfit; however, locking depths greater than 12 km do not offer significantly worse fit to the data overall.

calculations, unusually deep locking depths (>20 km) produce nearly identical fit to the data due to significantly different azimuths of the GPS and model predictions at the aforementioned distal and/or potentially unreliable sites. Thus, we conclude that the 13 km locking depth is most appropriate for matching GPS velocities in the region of fast contraction across the Ventura Basin. We explore the potential for variable locking depths later in the discussion section.

[38] The three-dimensional mechanical model produces surface motions that are similar to the GPS velocities, with the best-fitting model producing an average RMS error of 1.10 mm/yr (Figure 8) and an average horizontal residual magnitude of 0.89 mm/yr for all GPS sites. Due to our small estimated formal errors, few of the model velocities fit the GPS within 95% confidence limits, but we note that our average residual velocity is smaller than those from existing block models of the region. For example, the block models of *Meade and Hager* [2005] and *Loveless and Meade* [2011] produce average residuals of 1.26 and 1.67 mm/yr, respectively. Furthermore, block models tend to have relatively large residuals in the Transverse Ranges region [e.g., *McCaffrey*, 2005; *Meade and Hager*, 2005], suggesting that our model offers a better fit to the GPS data than existing models of the region. While many of the GPS velocities are matched well by the mechanical model predictions, mismatch between GPS and model predictions are typically largest at sites located far from the reference GPS site CIRX near the edge of the model domain (Figure 8b). This likely reflects one or more of the following factors: (1) spatial variations in regional rotation rates, (2) spatial variations in regional strain rates, (3) missing or inaccurately parameterized faults in the model, (4) inadequate parameterization of the model rheology, or (5) inaccurate GPS velocities. Implications of these sources of error and model results are explored later in the discussion section.

5.5. Interseismic Strain Rate Results

[39] Another test of the model that can be performed is to compare the model-predicted interseismic strain patterns to those derived from inverting the GPS velocity field. To calculate the model-predicted principal contraction rates, we use Poly3D to analytically calculate the principal strain rates and directions at the surface of the half-space for the best-fitting 13 km locking depth model. The results are reported on a grid identical to the GPS inversions, which allows calculation of the residuals between the model and GPS smoothed inversion results. Due to the limitations and smoothing of strain inversions, we focus our efforts on comparing the general patterns of the model-calculated and GPS inversion strain rate fields.

[40] The key feature of the GPS inversions is a belt of relatively fast strain rates localized around the Ventura Basin near the San Cayetano and Oak Ridge faults (Figure 5), which is reproduced to the first order by the model-calculated strain rate patterns (Figure 9). The model also predicts a counterclockwise rotation in principal contraction directions from north-northeast outside to north-northwest in the central Ventura Basin, which is generally consistent with the GPS strain inversions (cf. Figures 5 and 9). While the first-order strain rate patterns are reproduced by the model, analysis of the model residuals shows two main results (Figure 9b). First, the model produces contraction rates in the region around the Ventura Basin that are significantly slower than the GPS records. Second, the model produces faster strain rates than the GPS records away from the basin.

[41] An advantage of the model is that it can be used to predict spatial variations in strain rates in areas where there may be insufficient GPS data to provide a direct constraint. For example, the model predicts that the band of fast contraction across the Ventura Basin slows down and localizes around the Oak Ridge fault near the coastline but then increases and spreads out offshore following the trend of the Red Mountain fault in the Santa Barbara channel. While the GPS cannot reveal the details of the patterns of strain in the offshore due to sparse coverage, we can compare the total integrated strain of the GPS and the model across the Santa Barbara channel with the effects of regional rotation removed. Between sites ANA1 and CSST, the model predicts 6 mm/yr of N/S shortening while the GPS predicts 6.5 mm/yr of shortening. Between sites CRU1 and UCSB, the model predicts 6 mm/yr while the GPS measures 5 mm/yr of N/S convergence. Between sites MIG1 and TJRN, the model predicts 5.7 mm/yr of N/S convergence while the GPS data measures only 2.5 mm/yr. Therefore, the model produces increasing misfit with the GPS in the farther offshore regions to the west, but the model and GPS agree within ~1 mm/yr or less at longitudes east of site CRU1. Therefore, we expect that the zone of fast contraction produced by the model is likely present in the Santa Barbara channel, although possibly in subdued form in the western portion of the channel. The model also predicts that a band of relatively fast contraction should occur near the southeast edge of the region, near the Santa Monica and Malibu Coast faults. These zones of relatively fast strain rates arise due to relatively fast slip at depth on the otherwise locked Anacapa Dume, Malibu Coast, and Santa Monica faults. Given these results, offshore faults likely represent a significant and poorly understood hazard to the region.

[42] Because the model reproduces similar localization features to the GPS inversions, it is likely that the CFM contains the fastest slipping faults in the onshore portions of the western Transverse Ranges region. If there are active faults not represented in the CFM, they are most likely

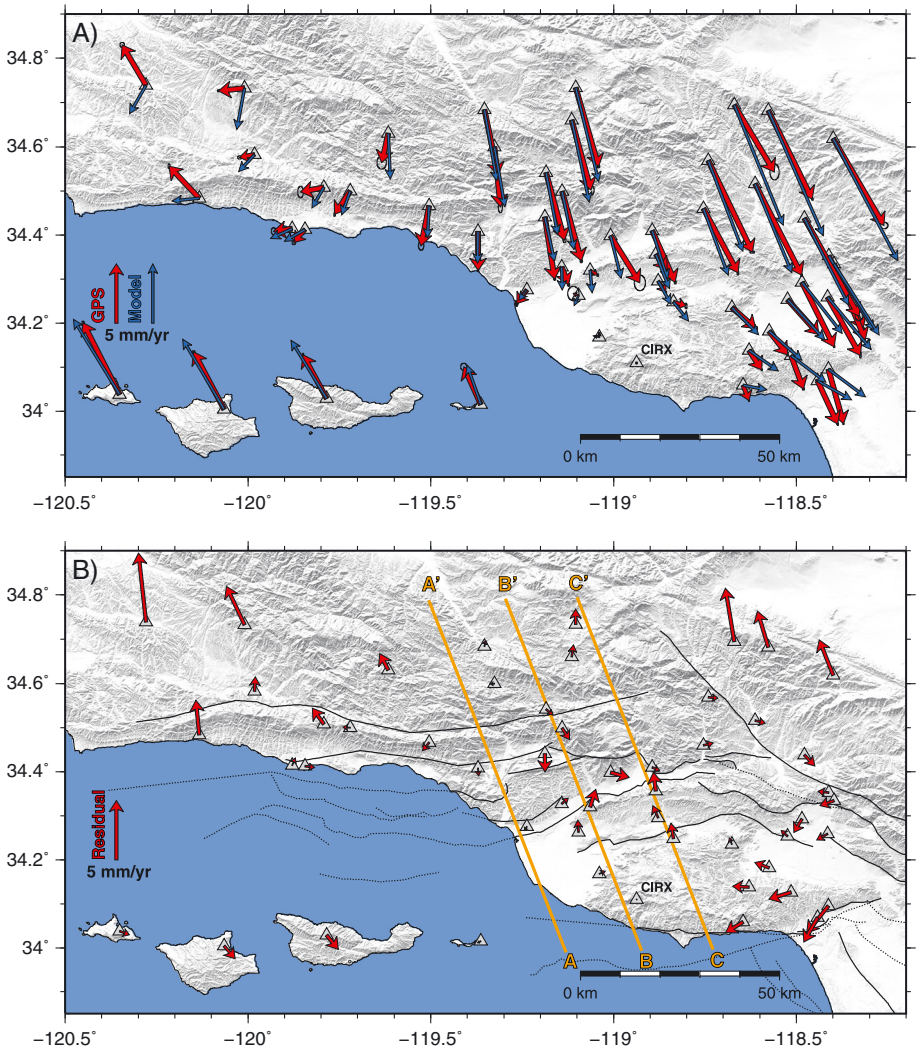

Figure 8. (a) Comparison of corrected interseismic GPS velocities (red vectors) to predictions from the three-dimensional mechanical model with a best-fitting 13 km locking depth (blue vectors). All velocities are shown relative to GPS site CIRX. (b) GPS-model residuals for the same 13 km locking depth model. Fault traces are shown with black sinuous lines that are dotted where blind or offshore. The green dotted line shows the approximate location of a potential unidentified fault not present in the CFM as noted in the discussion section. Note that in general, the model reproduces the GPS velocities well, with largest areas of misfit occurring near the edges of the region to the northwest, northeast, and southeast. Also, the model does not produce sufficiently fast velocity gradients across the Ventura Basin, a result that is expected because the model does not incorporate low-rigidity sediments [e.g., *Hager et al*. 1999].

located within the zones that are already identified as rapidly contracting, or relatively small in size and slowly slipping. We discuss the likelihood of the existence of unidentified faults and the likely effects of the model's homogeneous elastic structure later in this work.

6. Discussion

6.1. Variations in Regional Rotation Rates

[43] Given that the GPS-model residuals are often large at GPS sites far from station CIRX and many residuals appear to be approximately consistent with rotations about station CIRX, we investigate whether regional variations in rotation rates can at least partially explain the model misfit at the distal GPS sites. Because our main purpose here is to determine fault slip rates and to match the patterns of contraction, a detailed discussion of the potential geologic sources of rotation is beyond the scope of this work; however, we note that unlike strains, which are independent of reference frame, rotations are dependent on reference frame [e.g., *Lamb*, 1994].

[44] Our least squares inversion of the entire GPS data set estimated a regional rotation of $2.3 \pm 0.1°$/Myr in a clockwise sense. Using the same distance-weighted inversion given by equation (4), we can estimate the spatial variations in vertical axis rotation rates throughout the region (Figure 10). The distance-weighted inversion shows that the vast majority of the western Transverse Ranges region is experiencing clockwise vertical axis rotations. Many of the GPS sites in the far northwest and southeast (where GPS-model residuals are

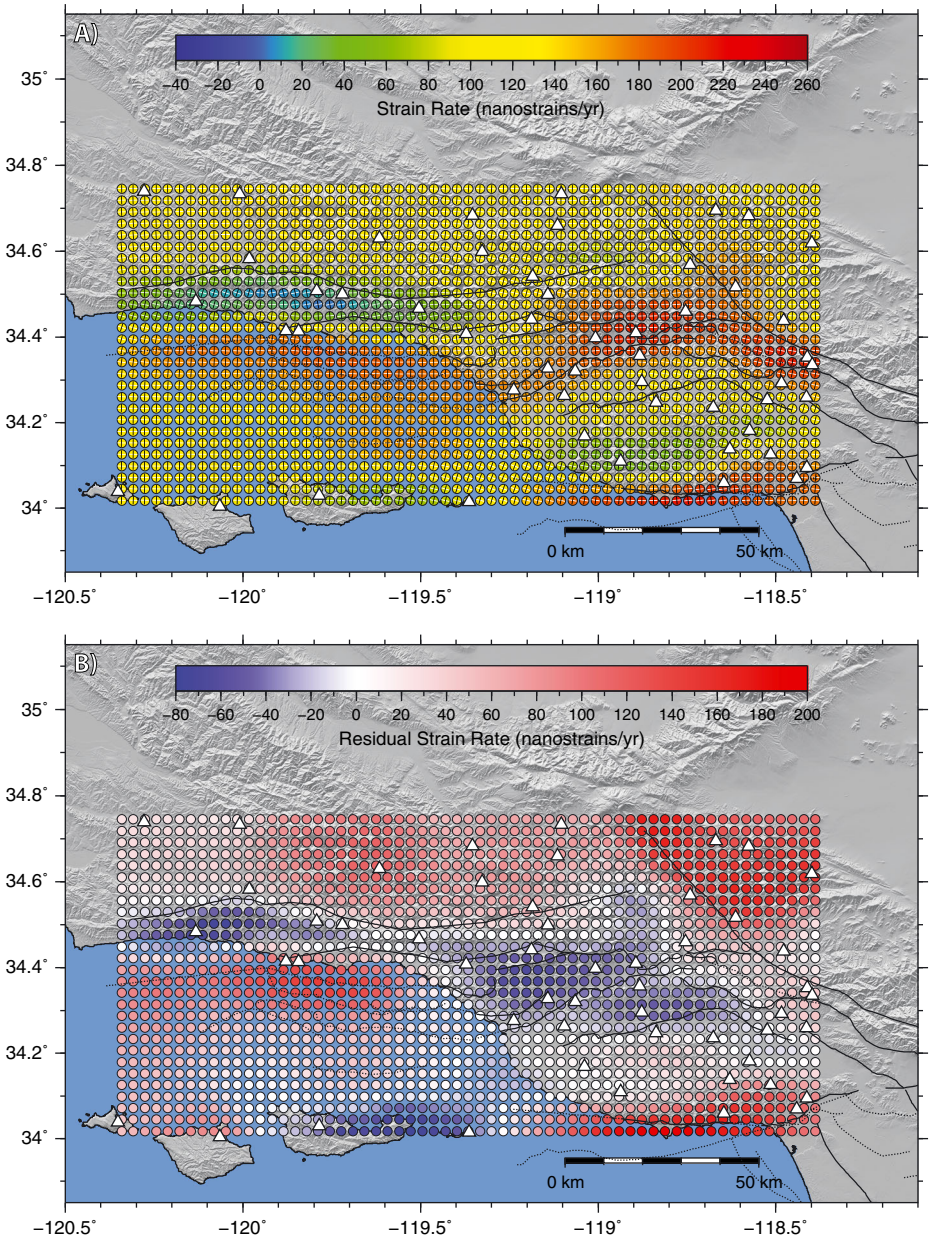

Figure 9. Variations in interseismic principal contraction rates and directions as predicted by the interseismic model with 13 km locking depth. All labeled features follow from Figure 5. Note that the patterns of fast strain across the Ventura Basin are similar to those calculated from inverting the GPS data (cf. Figure 5). The model suggests that the band of fast contraction across the Ventura Basin should continue offshore and follow the trend of the Red Mountain fault. Additionally, a zone of relatively fast contraction near the southeastern edge of the region is produced by deep slip on a combination of the Santa Monica, Malibu Coast, and Anacapa Dume faults. Such a feature cannot be resolved by the GPS due to a lack of offshore data. This cannot be resolved by the GPS data due to a lack of data in the Santa Barbara Channel.

relatively large) are predicted to be rotating at rates approximately double of the regional average rate. This implies that the best-fitting regional rotation rate is not likely to be representative of the motions observed at these sites and that the large residuals are therefore not surprising. Furthermore, the far southeast GPS sites are near the Los Angeles Basin, where *Marshall et al*. [2009] estimated significantly different tectonic boundary conditions. Thus, the regional boundary conditions applied here may not be representative of GPS velocities in the Los Angeles region.

6.2. One-Dimensional Profiles: Strengths and Weaknesses

[45] While the three-dimensional mechanical model presented here clearly matches the regional corrected horizontal GPS velocities to the first order, a commonly used approach is to select a linear transect though a region of interest and project the GPS data onto a one-dimensional profile [e.g., *Argus et al*., 2005; *Donnellan et al*., 1993a; *Hager et al*., 1999]. Projecting velocity data onto one-dimensional

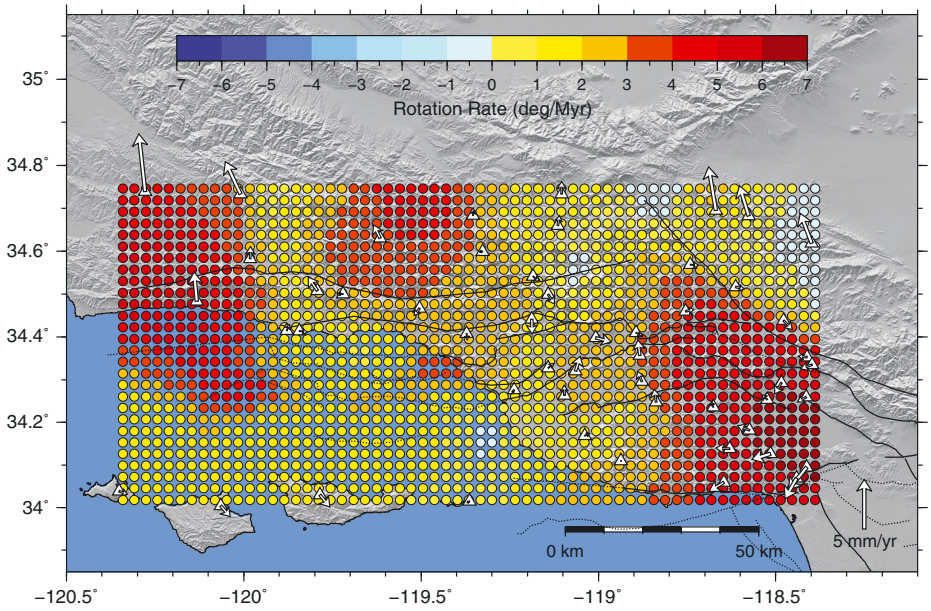

Figure 10. Variations in rotation rates throughout the region from a distance-weighted inversion of the GPS data (colored circles) and the model-GPS residuals (white arrows). Note that many of the large residuals are located in regions of the western Transverse Ranges that are rotating significantly faster than the best-fitting 2.3°/Myr rotation rate.

profiles removes the detailed two- and three-dimensional patterns shown in Figure 8 but facilitates identification of localized velocity gradients and offer a simple first-order method for estimating fault locations and slip rates. We therefore caution the reader that in a region of complex faulting with significant lateral variations in slip along faults, projecting GPS data onto linear profiles only offers a simplified and effectively first-order estimate of localized contraction rates and likely fault kinematics. We select three 95 km long N20°W transects through the GPS and model data (Figure 8b) and discuss the most likely cause of the observed localized fast contraction as well as the implications of analyzing one-dimensional transects in a region of complex three-dimensional faulting.

[46] Since the western Transverse Ranges contains the Ventura Basin, a thick accumulation of unconsolidated Pliocene sediments [*Yeats*, 1983], we also calculate the shear modulus values at depth for each transect to discuss the potential for localized contraction arising, in part, due to bedrock-sediment stiffness contrasts and not slip on faults. Shear modulus values are derived from V_p, V_s, and density values provided by the SCEC Community Velocity Model (CVM) version 4.0 [*Kohler et al.*, 2003; *Magistrale et al.*, 2000].

6.2.1. Homogeneous Elastic Half-space Models

[47] The N20°W velocities along transect A show a somewhat diffuse pattern of contraction that agrees relatively well with the mechanical model predictions (Figures 11–13). Because deformation in the three-dimensional mechanical model is partitioned between elastic deformation due to slip on faults (including folding above blind faults) and elastic deformation due to the applied regional shortening that is not released by faulting (because the faults are disconnected and finite in extent), most regions of the model produce approximately linear velocity gradients (Figures 11–13), and zones of localized contraction are quite subtle compared to the GPS velocity gradients. While one could interpret a relatively localized zone of contraction between GPS sites OVLS and HVYS, given the lack of stations between these sites, it is not clear exactly how localized the contraction is across the Ventura Basin near the coastline. Therefore, given the somewhat diffuse GPS spacing, the mechanical model appears to agree at least to the first order with the contraction rates across the Ventura Basin near the coastline.

[48] Alternatively, using the solutions of *Okada* [1985], we run a suite of simple forward models of planar dislocations and adjust parameters to attain a visual fit with the horizontal GPS data in transect A. Fault length is tested in 10 km increments, fault slip rate in 0.5 mm/yr increments, and locking depth in 1 km increments. Because we will argue below that these models are fundamentally flawed, we do not formally invert the GPS data for the fault parameters.

[49] The horizontal GPS data in transect A fit well with a single 250 km long rectangular dislocation with 12 mm/yr of slip and a 7 km locking depth. The dislocation length is effectively a minimum; longer dislocations fit the data nearly equally well. This hypothetical fault approximately coincides with the location of the Red Mountain fault, which suggests that the Red Mountain fault in the CFM is in approximately the correct location to produce the GPS-measured contraction gradient. While the simplicity of this kinematic dislocation model may be appealing when attempting to fit the GPS data, we argue that this or similar simple kinematic dislocation models are implausible for three reasons: (1) the locking depth required to fit the data is too shallow, given observations of slip at ~20 km depth in the 1994 Northridge earthquake [*Hager et al.*, 1999; *Hudnut et al.*, 1996] and a lack of any sheared boreholes to at least 3 km depth throughout the region [*Donnellan et al.*, 1993a]; (2) the simple dislocation model predicts a significant uplift gradient across the basin, which is not observed in the GPS data (Figure 11c); and (3) this model assumes that slip on the Red Mountain fault at

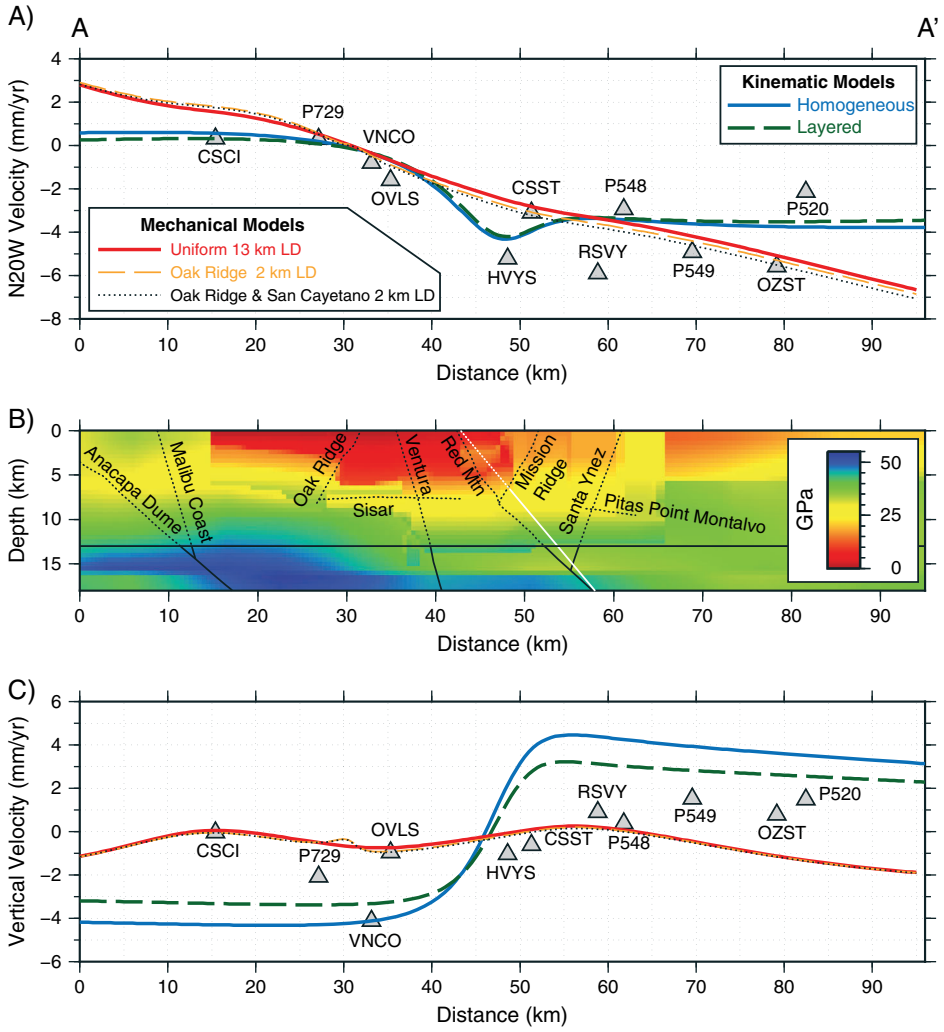

Figure 11. N20°W profile A-A' (see Figure 8 for location) with 0 km distance at the southeast end of the transect. GPS sites within 18 km of the transect are shown here with the N20°W component of velocity plotted. (a) One-dimensional transect through the horizontal GPS velocity data (gray triangles), three-dimensional mechanical model with a 13 km locking depth (red curve), a homogeneous elastic half-space rectangular dislocation model of a hypothetical fault with 12 mm/yr of slip and a 7 km locking depth (blue curve), a layered elastic half-space model with 9 mm/yr of slip and a 7 km locking depth (green dashed curve), and models with shallow 2 km locking depth on the basin-bounding San Cayetano and Oak Ridge faults (yellow dashed, and black dotted curves). (b) CFM fault structure (black lines, dotted where locked) and shear modulus values (color scale) derived from the SCEC CVM version 4.0. The best-fitting 13 km locking depth from the mechanical model is shown with a horizontal black line and a hypothetical rectangular dislocation dipping 50° northward is shown with a white line. The dashed portion of the white line shows the projection of the dislocation to the surface of the Earth. (c) Vertical GPS velocities (triangles) and predictions from the three-dimensional mechanical model and kinematic dislocation models following the same color scheme as in Figure 11a. In Figures 11a and 11c, GPS formal error bars are typically much smaller than the triangle symbols, so they are omitted to avoid cluttering the figure.

depth is faster than geologic estimates (cf. Figure 6) and is the only process responsible for the GPS-measured contraction. Deformation-inducing processes such as aseismic fold growth [e.g., *Yeats et al*., 1988], off-fault deformation in general (elastic or permanent), and deformation due to the other known active faults are not accounted for. In contrast, the mechanical model utilizes a deeper and more reasonable 13 km locking depth, produces a negligible amount of uplift across the basin, and predicts geologically reasonable slip rates on nearly all faults in the region. The mechanical model could remain consistent with the GPS data with additional slip on the Red Mountain or Ventura faults; however, because the mechanical model predicts slip rates that are compatible with the applied tectonic regional strain rate, faster slip on these faults is only mechanically feasible if the faults were longer or more connected than suggested by the SCEC CFM. Later, we discuss the possibility that the misfit between the mechanical model and the GPS is dominantly due to the homogeneous elastic structure and not missing or incorrectly slipping faults.

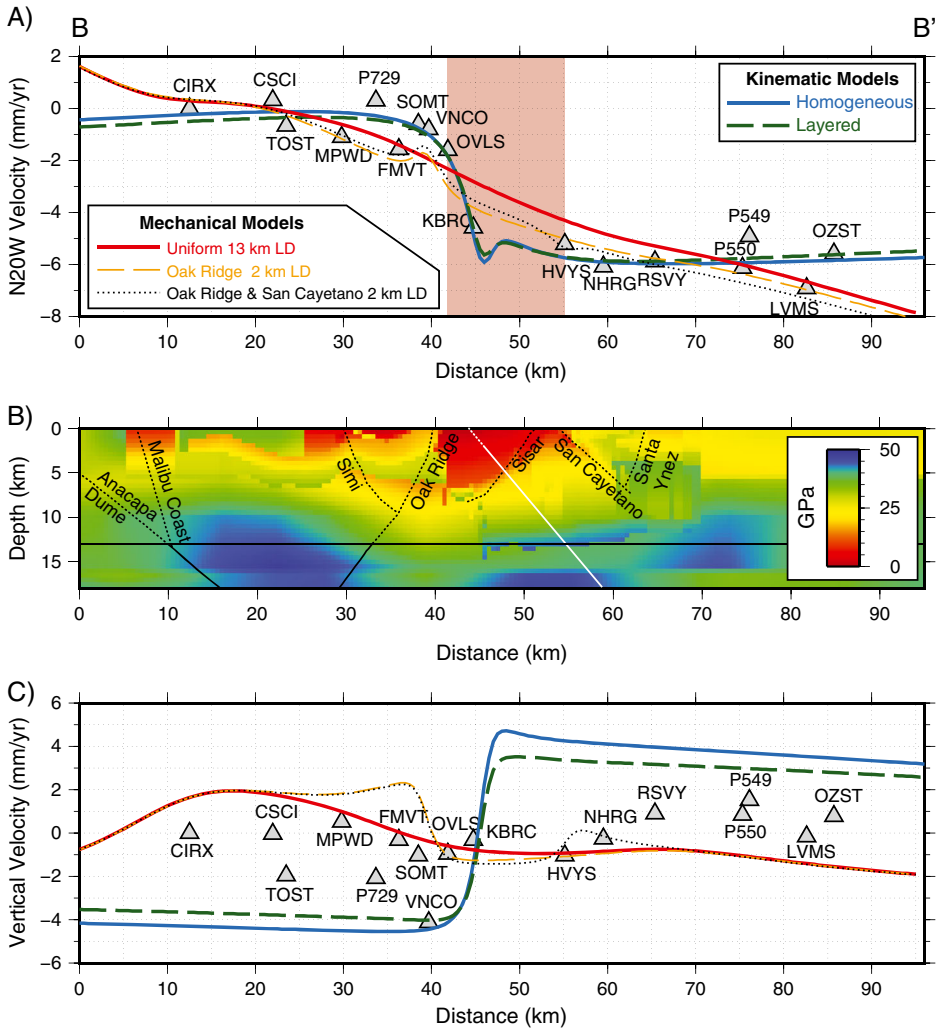

Figure 12. N20°W profile B-B' (see Figure 8 for location) with 0 km distance at the southeast end of the transect. Labeled features follow from Figure 11. The rectangular dislocation model for a hypothetical fault shown here (blue curve) has 12 mm/yr of slip and a 2 km locking depth and dips northward at 50°. Note that this hypothetical fault does not align with any faults in the SCEC CFM. Because the zone of fast contraction (highlighted with a pale red rectangle) approximately coincides with the region of low-modulus basin fill, fast contraction rates could also be produced by rock stiffness contrasts. A layered elastic half-space dislocation model (green dashed curve) shown here has 10 mm/yr of slip and a 2 km locking depth.

[50] The N20°W velocities along transects B and C show a zone of contraction that is significantly more localized than in transect A (Figures 12 and 13). In transect B, the zone of fast contraction is located between GPS sites OVLS and HVYS, and in transect C, the zone of fast contraction lies between SOMT and KBRC, although we note that given the gap in the GPS site locations, the zone of fast contraction in transect C could extend farther north than what is indicated in Figure 13b. The mechanical model with 13 km locking depth does not produce a zone of shortening as localized as the GPS data suggest in either of these two transects. Following the same procedure as in transect A, a 250 km long rectangular dislocation model of a hypothetical fault with a slip rate of 12 mm/yr and a 2 km locking depth matches well the horizontal GPS data in both remaining transects. We note that while the location of this hypothetical fault does not correspond to any fault in the CFM, it is similar to the location suggested for the South San Cayetano fault of *Hubbard et al.* [submitted to *Bulletin of the Seismological Society of America*, 2013], which is not currently included in the SCEC CFM.

[51] While the simple kinematic dislocation models of transects B-C match the horizontal GPS data better than the mechanical model, we argue that these simplified models are problematic, for similar reasons mirroring those described in transect A: (1) the locking depth is unrealistically shallow; (2) the uplift gradient produced by this hypothetical fault is ~9 mm/yr whereas the GPS shows essentially no uplift gradient across the basin; and (3) a slip rate of 12 mm/yr exceeds the geologic estimates for the Oak Ridge and San Cayetano faults (cf. Figure 6). Further complicating the issue, the zone of fast contraction in both transects B and C coincides with a thick package of low-rigidity sediments, suggesting that variations in rock stiffness, not slip on faults, at least partially or possibly nearly entirely explain the zone of fast contraction at this location [e.g., *Hager et al.*, 1999]. For example, if we

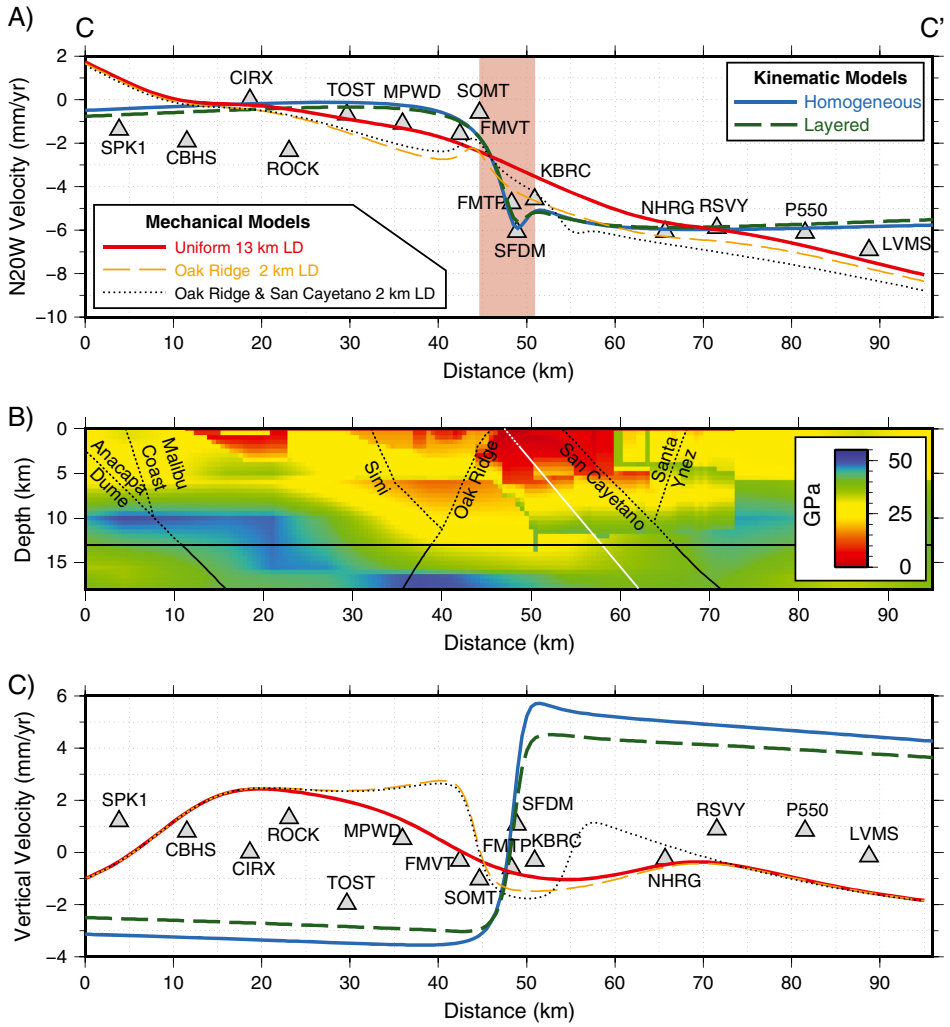

Figure 13. N20°W profile C-C' (see Figure 8 for location) with 0 km distance at the southeast end of the transect. Labeled features follow from Figure 11. The rectangular dislocation model for a hypothetical fault shown here (blue curve) has 12 mm/yr of slip and a 2 km locking depth and dips northward at 50°. Note that this hypothetical fault does not align with any faults in the SCEC CFM. Because the zone of fast contraction (highlighted with a pale red rectangle) approximately coincides with the region of low-modulus basin fill, fast contraction rates could also be produced by rock stiffness contrasts. A layered elastic half-space dislocation model (green dashed curve) shown here has 10 mm/yr of slip and a 2 km locking depth.

compare the shear modulus values calculated from the SCEC Community Velocity Model (Figure 14) to the model strain rate residuals (Figure 9b), we see that there is a strong correspondence between low-modulus sediments and the model residuals. This suggests that the inability of the mechanical model to produce strong localizations in strain may be dominantly controlled by the model's inadequate homogeneous elastic structure and not incorrect fault slip. The prevalence of positive residuals (indicating too much elastic strain off the faults in the model) is likely a consequence of the CFM having a fault network that is insufficiently connected. Therefore, while the mechanical model fails to reproduce the highly localized zone of contraction, we suggest that this is due to a combination of rock stiffness variations not included in the model as well as a potentially active fault not included in the SCEC CFM. Determining the exact relative contributions of all of the region's faults, including the South San Cayetano fault, along with the rock stiffness variations is nontrivial and requires a full mechanical modeling effort using a more complex modeling technique such as the finite element method. Nonetheless, we next explore the basic first-order effects of a near-surface compliant material (i.e., lower shear modulus) using a series of layered elastic half-space dislocation models and discuss the implications.

6.2.2. Layered Elastic Half-Space Models

[52] The shear modulus values inferred from seismic velocities [*Kohler et al.*, 2003; *Magistrale et al.*, 2000] show that the Ventura Basin near the coast is rather broad, with low-modulus sediments near the surface down to ~5 km depth, while to the west, the basin has a more localized and irregular shape (Figures 11–14). Numerous existing studies have shown that low-modulus, near-surface material can greatly affect resultant surface deformation around slipping faults [e.g., *Fay and Humphreys*, 2005; *Fialko*, 2006; *Fukahata and Matsu'ura*, 2005; *Hager et al.*, 1999; *Savage*, 1998; *Schmalzle et al.*, 2006; *Wang et al.*, 2003].

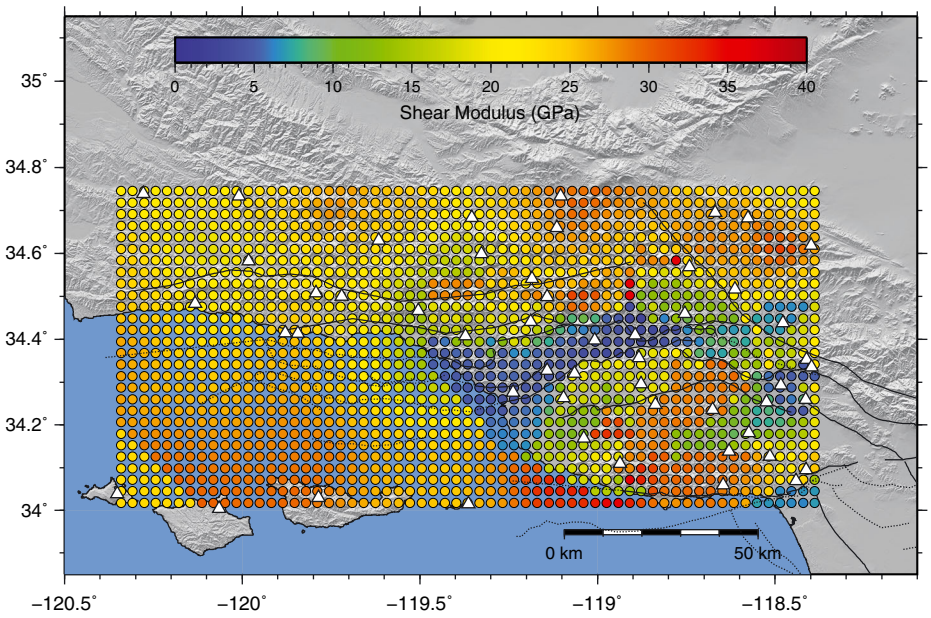

Figure 14. Shear modulus values calculated from the SCEC Community Velocity Model version 4.0 [*Kohler et al*., 2003; *Magistrale et al*., 2000] at a depth of 2 km plotted on the same grid as the strain rate maps presented earlier (Figures 5 and 9). Depth slices <5 km deep yield similar results. The zone of low rigidity near the center of the map is due to unconsolidated sediments in the Ventura Basin. The abrupt termination of the low-modulus zone in the offshore is due to a lack of resolution in the seismic velocity model in the offshore region and is artificial. Note that the zone of low-rigidity sediments closely correspond to the regions where the mechanical model predicts strain rates that are too slow compared to the GPS data (Figure 9b), suggesting that the model-GPS misfit is at least partially due to the simple homogeneous elastic properties of the mechanical model.

To investigate the first-order effects of these low-modulus sediments on interseismic deformation patterns, we present results from kinematic dislocation models that incorporate a layered elastic half-space using the solutions of *Fukahata and Matsu'ura* [2005]. In all models presented here, the layered half-space contains two horizontal layers. The upper layer has a shear modulus of 10 GPa, a Poisson's ratio of 0.25, and a thickness of 5 km. The lower layer has a shear modulus of 30 GPa and an identical Poisson's ratio of 0.25. The geometry of the fault in the homogeneous and layered models are identical (same dip and locking depth). Therefore, other than the rheologic layering, the only difference between the homogeneous and heterogeneous kinematic models are the slip rates. Fault parameters in the layered elastic forward models are determined using the same procedure as in the homogeneous dislocation models.

[53] Along transect A, we are able to achieve a nearly identical fit to the horizontal GPS data compared to the homogeneous kinematic model with a slip rate of only 9 mm/yr (Figure 11a). This is a 25% reduction compared to the homogeneous model's 12 mm/yr of slip, which results from the presence of low-modulus material near the surface that helps to localize the deformation compared to a homogeneous rheology. The 9 mm/yr of slip still exceeds the geologic estimates of slip on the Red Mountain fault (cf. Figure 6) but is an improvement over the homogeneous model's 12 mm/yr of slip. An added benefit of the layered model is that the uplift gradient generated is significantly less (due to a slower slip rate), although the model still produces an uplift gradient that does not agree with the GPS data (Figure 11c).

[54] Layered elastic half-space models show similar improvements over the homogeneous kinematic models for transects B-C. In both transect B and transect C, the slip rate of the layered elastic half-space models is reduced to 10 mm/yr, yet the fit to the horizontal GPS data is nearly identical (Figures 12a and 13a). This 17% reduction in slip rate compared to the homogeneous kinematic model still requires slip rates beyond geologic estimates on the San Cayetano or Oak Ridge faults. Furthermore, this reduction in slip once again results in a smaller uplift gradient across the basin; however, the uplift gradient produced by the layered elastic models still greatly exceeds the uplift measured by GPS (Figures 12c and 13c).

[55] In the end, the layered elastic half-space models produce results that agree better with GPS and geologic data compared to the homogeneous kinematic models, but neither set of kinematic models fits all of the available data (GPS and geologic slip rate data) as well as the mechanical model. While the layered elastic models presented here only incorporate two horizontal layers with differing shear moduli, the actual structure of the Ventura Basin is far more complex than a simple two-layered model, and the effects of this material contrast in a three-dimensional mechanical model are unknown. Future efforts should focus on a full three-dimensional heterogeneous modeling effort to determine the relative importance of the variations in rock stiffness throughout the western Transverse Ranges.

6.3. Locking Depth Implications

[56] The best-fitting and uniform locking depth of 13 km (determined earlier) is significantly deeper than the 5 km

locking depth determined by *Donnellan et al*. [1993a], slightly shallower than the 15 km locking depth modeled by *Hager et al*. [1999], and shallower than the model-based estimates of slip down to 19 km depth during the Northridge earthquake [*Hudnut et al*., 1996; *Wald et al*., 1996]. The best-fitting locking depth of 13 km may seem too shallow given the depth of coseismic slip in the Northridge earthquake; however, it is has been suggested that some coseismic slip may occur below a fault's locking depth [*Shaw and Scholz*, 2001; *Shaw and Wesnousky*, 2008]. Therefore, it is possible that the faults are locked at ~13 km depth, but moderate to large earthquakes may partially rupture portions of faults below the locking depth. Alternatively, because the deformation patterns created by faults embedded in low-modulus, near-surface material are, in many cases, indistinguishable from homogeneous models [*Savage*, 1998], the assumption of homogeneous material properties in the numerical models may yield a locking depth that is too shallow [e.g., *Hager et al*., 1999; *Savage*, 1998].

[57] The main shortcoming of the mechanical model is the inability to produce sufficiently fast contraction rates across the Ventura Basin. We now explore whether a shallower locking depth on the basin-bounding faults can improve fit to the GPS data. To accomplish this, we apply the best-fitting 13 km locking depth to all faults except for the basin-bounding San Cayetano and Oak Ridge faults, which are given a 2 km locking depth (identical to the locking depth of the best-fitting rectangular dislocation models). Experiments with altering other fault locking depths near or in the Ventura Basin, including the Red Mountain, Ventura, and Sisar faults, resulted in negligible changes in the profiles shown in Figures 11–13. We note that altering the locking depth of the Red Mountain fault does significantly affect the deformation rates in the offshore region (where slip rates are fast), but near the coast and transect A, the Red Mountain fault terminates and is therefore slowly slipping in the mechanical models.

[58] Shallow 2 km locking on the Oak Ridge and/or San Cayetano faults produces only negligible changes to the patterns of convergence in transect A (Figure 11). This occurs because the San Cayetano fault does not cross transect A, and the Oak Ridge fault is dominantly strike slip and slowly slipping at the longitude of transect A. In transects B-C (Figures 12 and 13), the shallower locking depth produces a better match to the GPS-measured horizontal contraction rate, but like the simple dislocation models presented earlier, mismatch with the vertical GPS data is significantly increased. When only the Oak Ridge fault is shallowly locked, the south side of the basin uplifts faster than the north end. When both faults are shallowly locked, a horst and graben style uplift pattern is produced. Neither of these uplift patterns are consistent with the vertical GPS data, so we conclude that a very shallow locking depth on the San Cayetano and/or Oak Ridge faults is not likely. The lack of sufficiently fast contraction in the mechanical model is therefore most likely due to an inadequate homogeneous elastic structure.

6.4. Determining Accurate Slip Rates Requires Detailed Fault Geometry

[59] When comparing geologic slip rate estimates to slip rates estimated from models with simple geometries (block and two-dimensional models), the simplified models often produce slip rates that are significantly different than geologic estimates. For example, existing two-dimensional models included only the San Cayetano and Oak Ridge faults, and in order to match the geodetic data, 7.8 ± 1.6 mm/yr [*Hager et al*., 1999] and 8.0 ± 2.0 mm/yr [*Donnellan et al*., 1993a] of slip were required on each fault. This is inconsistent with geologic estimates of <5 mm/yr on the Oak Ridge fault. Furthermore, these two-dimensional models both modeled the San Cayetano and Oak Ridge faults as being parallel and 4–7 km apart at the surface. Inspection of the CFM fault geometry in Figure 1 suggests that this is not a reasonable geometrical approximation of these two faults because the faults are only closely spaced in the central Ventura Basin and then diverge in both directions. Block modeling results of *Meade and Hager* [2005] and *Loveless and Meade* [2011] match some geologic slip rate estimates well, but both block models predict normal slip on the Santa Monica fault, which is inconsistent with well-constrained geologic data suggesting significant reverse slip [*Davis and Namson*, 1989, 1994; *Dolan and Pratt*, 1997; *Dolan et al*., 2000b; *Tsutsumi et al*., 2001]. In the end, the slip rates determined from modeling geodetic data ultimately depend on the assumptions (primarily the fault geometry) of the model. Thus, a good fit to the geodetic data alone is nonunique and does not necessarily produce reliable geologic slip rate estimates.

6.5. Implications for the Community Fault Model and Seismic Hazard Assessment

[60] While the CFM fault geometries throughout the Transverse Ranges appear to produce slip rates and slip distributions that are largely consistent with geologic estimates [*Marshall et al*., 2008, 2009; *Meigs et al*., 2008], the CFM-based mechanical model presented here fails to localize enough regional strain into slip on faults. If the CFM faults were more connected and provided a longer and more throughgoing fault surface following the trend of the Ventura Basin, more of the regional shortening would be released by slip on faults (similar to a 2D dislocation model). Given the complex fault network of relatively short and unconnected fault surfaces in the current CFM, it is expected that each fault will produce only small perturbations from a linear velocity gradient, which does not agree with highly localized contraction across the Ventura Basin. For a mechanical model using the CFM geometries to better match the available geodetic data, the results here suggest that there must be a fault or series of connected fault surfaces that form at least a 250 km long throughgoing surface in order for regional shortening to be released as slip on faults.

[61] If the faults of the western Transverse Ranges are locked down to 13 km or more and are as disconnected as the CFM suggests, many of the CFM fault surfaces will produce negligible interseismic deformation in an elastic model. This occurs because the CFM fault network contains several faults that are subordinate and are truncated by more major faults (see the supporting information for the full three-dimensional fault geometry), resulting in no fault surface below the locking depth. Furthermore, because many of the faults in the region are disconnected and slowly slipping, their perturbation to the regional interseismic velocity field is negligible. Thus, the regional interseismic deformation patterns are dominantly controlled by only a few major faults. Given the mechanical model results and the current CFM fault configuration, the Red Mountain,

Anacapa Dume, Oak Ridge, and San Cayetano faults (in no particular order) appear to be the dominant drivers of interseismic deformation throughout the region. Conversely, given the best-fitting 13 km locking depth, the Pitas Point Montalvo, North Channel, Mission Ridge, Sisar, and Simi faults all have no fault surface below the 13 km locking depth and consequently do not contribute to the interseismic deformation field. Coseismic events on these faults may be driven by stress changes due to deep interseismic creep on the other more major nearby faults or by regional shortening in general. This implies that the western Transverse Ranges may contain several active faults that produce essentially no measurable interseismic deformation, and other unidentified active faults may be present but are not detectable using interseismic geodetic data. If true, this poses a significant difficulty for seismic hazard analyses based on interseismic deformation patterns.

7. Conclusions

[62] In contrast to the nearby Los Angeles Basin, nontectonic motions in the western Transverse Ranges region are generally not a significant source of error in tectonic GPS velocity estimates for most permanent GPS stations in the region. While we have identified several locations of likely anthropogenic motion, the vast majority of these sites contain no permanent GPS stations. The only exception is GPS site P729, which likely has a westward component of anthropogenic. Ongoing hydrocarbon production along the Ventura Avenue anticline produces highly localized subsidence that is not likely to contaminate GPS-measured velocities in the region. Thus, the vast majority of permanent GPS sites throughout the region should yield accurate tectonic velocities.

[63] Using a model driven by geodetically determined strain rates, we show that there are not any significant discrepancies between short-term slip rates captured by geodesy and longer-term slip rates measured by geology. Previous GPS-derived slip rate estimates likely incorrectly estimated fault slip rates due to oversimplifications in fault geometry, and some geologic estimates of slip were likely made in nonrepresentative locations along faults, thereby incorrectly suggesting a mismatch between short- and long-term slip rates. Therefore, significant temporal shifts in strain rates [e.g., *Dolan et al*., 2007] need not be evoked to fit both the geologic and geodetic data in the western Transverse Ranges region.

[64] Inversions of GPS data for strain rates show a clear belt of fast contraction across the Ventura Basin, which is likely due to a combination of deep slip on buried faults and heterogeneous off-fault deformation related to the low-rigidity sediments of the Ventura Basin [e.g., *Hager et al*., 1999]. While the mechanical model presented here does not reproduce the magnitudes of fast contraction rates in the central Ventura Basin, the missing strain is most likely due to the homogeneous elastic structure modeled. Simple dislocation models can match the fast and localized strain rates, but such models require anomalously shallow locking depths and produce large uplift gradients that are inconsistent with the GPS data. Furthermore, the zones of fast contraction appear to approximately coincide with zones of very low shear modulus basin fill, suggesting that a significant portion of the fast and localized contraction in the Ventura Basin is due to heterogeneous rock stiffness and not deep slip on faults. Although we cannot rule out the possibility of additional active faults of modest slip rates (~5 mm/yr or less) being present within the Ventura Basin [e.g., *Hubbard et al*., submitted to *Bulletin of the Seismological Society of America*, 2013], the GPS data show no significant vertical uplift gradients across the basin. The missing contraction in the mechanical models presented here compared to GPS is most likely dominantly due to the simple homogeneous rheology of the model and not incorrect slip rates or missing faults. While the mechanical model does not produce zones of contraction across some sections of the Ventura Basin that are as localized as the GPS data predict, we argue that the mechanical model is nonetheless an improvement over existing two-dimensional models because the mechanical model honors the complex three-dimensional geologic fault structure, agrees well with nearly all long-term fault slip rates, matches well the first-order patterns of horizontal and vertical GPS velocities, and reproduces the first-order patterns of regional strain measured by geodesy.

[65] Mechanical models predict two zones of localized fast contraction rates that cannot be accurately resolved given the current GPS network station distribution. The model-predicted zones of fast contraction lie in the Santa Barbara channel following the trend of the Red Mountain fault, along with a zone of fast contraction that follows the trend of the Malibu Coast and Anacapa Dume faults just offshore from Santa Monica. These zones of fast contraction indicate that offshore faults may pose a significant, yet currently poorly understood, seismic hazard to the region.

[66] **Acknowledgments.** This work benefitted from constructive reviews from two anonymous reviewers. All figures were made with Generic Mapping Tools [*Wessel and Smith*, 1998]. Focused SAR images were produced using the ROI_PAC software package developed by the Jet Propulsion Laboratory. Interferograms were formed using the DORIS software package developed by the Delft University of Technology. The StaMPS software package was provided by Delft University. Envisat data was provided by UNAVCO and the WINSAR consortium. The MEaSUREs GPS time series data and the QOCA software package were provided by the Jet Propulsion Laboratory. This research was supported by the Southern California Earthquake Center. SCEC is funded by NSF Cooperative Agreement EAR-0529922 and USGS Cooperative Agreement 07HQAG0008. The SCEC contribution number for this paper is 1744.

References

Allmendinger, R. W., R. Reilinger, and J. P. Loveless (2007), Strain and rotation rate from GPS in Tibet, Anatolia, and the Altiplano, *Tectonics*, *26*, TC3013, doi:10.1029/2006TC002030.

Allmendinger, R. W., J. P. Loveless, M. E. Pritchard, and B. J. Meade (2009), From decades to epochs: Spanning the gap between geodesy and structural geology of active mountain belts, *J. Struct. Geol.*, *31*, 1409–1422.

Allmendinger, R. W., N. Cardozo, and D. M. Fisher (2012), *Structural Geology Algorithms: Vectors and Tensors*, Cambridge University Press, New York, NY.

Argus, D. F., M. B. Heflin, G. Peltzer, F. Crampé, and F. H. Webb (2005), Interseismic strain accumulation and anthropogenic motion in metropolitan Los Angeles, *J. Geophys. Res.*, *110*, B04401, doi:10.1029/2003JB002934.

Azor, A., E. A. Keller, and R. S. Yeats (2002), Geomorphic indicators of active fold growth; South Mountain-Oak Ridge Anticline, Ventura Basin, Southern California, *Geol. Soc. Am. Bull.*, *114*(6), 745–753.

Baldwin, J. N., K. I. Kelson, and C. E. Randolph (2000), Late Quaternary fold deformation along the Northridge Hills Fault, Northridge, California: deformation coincident with past Northridge blind thrust earthquakes and other nearby structures?, *Bull. Seismol. Soc. Am.*, *90*(3), 629–642.

Bawden, G. W., W. Thatcher, R. S. Stein, K. W. Hudnut, and G. Peltzer (2001), Tectonic contraction across Los Angeles after removal of groundwater pumping effects, *Nature*, *412*, 812–815.

Becker, T. W., J. L. Hardebeck, and G. Anderson (2005), Constraints on fault slip rates of the southern California plate boundary from GSA velocity and stress inversions, *Geophys. J. Int.*, *160*, 634–650.

Bürgmann, R., M. E. Ayhan, E. J. Fielding, T. J. Wright, S. McClusky, B. Aktug, C. Demir, O. Lenk, and A. Türkezer (2002), Deformation during the 12 November 1999 Düzce, Turkey, Earthquake, from GPS and InSAR Data, *Bull. Seismol. Soc. Am.*, *92*(1), 161–171.

Carena, S., and J. Suppe (2002), Three-dimensional imaging of active structures using earthquake aftershocks: The Northridge thrust California, *J. Struct. Geol.*, *24*, 887–904.

Çemen, I. (1989), Near-surface expression of the eastern part of the San Cayetano fault: A potentially active thrust fault in the California Transverse Ranges, *J. Geophys. Res.*, *94*(B7), 9665–9677.

Cooke, M. L., and L. C. Dair (2011), Simulating the recent evolution of the southern big bend of the San Andreas fault, southern California, *J. Geophys. Res.*, *116*, B04405, doi:10.1029/2010JB007835.

Cooke, M. L., and S. T. Marshall (2006), Fault slip rates from three-dimensional models of the Los Angeles metropolitan area, California, *Geophys. Res. Lett.*, *33*, L21313, doi:10.1029/2006GL027850.

Dair, L., and M. L. Cooke (2009), San Andreas fault geometry through the San Gorgonio Pass, California, *Geology*, *37*(2), 119–122.

Davis, T. L., and J. S. Namson (1989), Structural transect of the western Transverse Ranges, California; Implications for lithospheric kinematics and seismic risk evaluation; reply, *Geology*, *17*(4), 377.

Davis, T. L., and J. S. Namson (1994), A balanced cross-section of the 1994 Northridge earthquake, southern California, *Nature*, *372*, 167–169.

Dieterich, J. H., and D. E. Smith (2009), Nonplanar faults: Mechanics of slip and off-fault damage, *Pure Appl. Geophys.*, *166*, 1799–1815.

Dolan, J. F., and T. L. Pratt (1997), High-resolution seismic reflection profiling of the Santa Monica fault zone, west Los Angeles, California, *Geophys. Res. Lett.*, *24*(16), 2051–2054.

Dolan, J. F., K. Sieh, T. K. Rockwell, P. Guptill, and G. Miller (1997), Active tectonics, paleoseismology, and seismic hazards of the Hollywood fault, Los Angeles basin, California, *Geol. Soci. Am. Bull.*, *109*(12), 1595–1616.

Dolan, J. F., K. Sieh, T. K. Rockwell, R. Yeats, J. H. Shaw, J. Suppe, G. J. Huftile, and E. M. Gath (1995), Prospects for larger or more frequent earthquakes in the los angeles metropolitan region, *Science*, *267*, 199–205.

Dolan, J. F., D. Stevens, and T. K. Rockwell (2000a), Paleoseismic evidence for an early to mid-Holocene age of the most recent surface rupture on the Hollywood fault, Los Angeles, California, *Bull. Seismol. Soc. Am.*, *90*(2), 334–344.

Dolan, J. F., K. Sieh, and T. K. Rockwell (2000b), Late Quaternary activity and seismic potential of the Santa Monica fault system Los Angeles, California, *Geol. Soc. Am. Bull.*, *112*, 1559–1581.

Dolan, J. F., D. D. Bowman, and C. G. Sammis (2007), Long-range and long-term fault interactions in southern California, *Geology*, *35*(9), 855–858.

Dong, D., T. Herring, and R. King (1998), Estimating regional deformation from a combination of space and terrestrial geodetic data, *J. Geod.*, *72*, 200–214.

Dong, D., P. Fang, Y. Bock, F. H. Webb, L. Prawirodirdjo, S. Kedar, and P. Jamason (2006), Spatiotemporal filtering using principal component analysis and Karhunen-Loeve expansion approaches for regional GPS network analysis, *J. Geophys. Res.*, *111*, B03405, doi:10.1029/2005JB003806.

Donnellan, A., B. H. Hager, and R. W. King (1993a), Discrepancy between geological and geodetic deformation rates in the Ventura Basin, *Nature*, *366*, 333–336.

Donnellan, A., B. H. Hager, R. W. King, and T. A. Herring (1993b), Geodetic measurement of deformation in the Ventura Basin region, Southern California, *J. Geophys. Res.*, *98*(B12), 727–721.

Fay, N. P., and E. D. Humphreys (2005), Fault slip rates, effects of elactic heterogeneity on geodetic data, and the strength of the lower crust in the Salton Trough region, southern California, *J. Geophys. Res.*, *110*, B09401, doi:10.1029/2004JB003548.

Ferretti, A., C. Prati, and F. Rocca (2001), Permanent scatterers in SAR interferometry, *IEEE Trans. Geosci. Remote Sens.*, *39*(1), 8–20.

Fialko, Y. (2006), Interseismic strain accumulation and the earthquake potential on the southern San Andreas fault system, *Nature*, *441*, 968–971.

Field, E. H., et al. (2007), The Uniform California Earthquake Rupture Forecast, Version 2 (UCERF 2), USGS Open File Report 2007–1437, US Geological Survey, Menlo Park, CA.

Freund, L. B., and D. M. Barnett (1976), A two-dimensional analysis of surface deformation due to dip-slip faulting, *Bull. Seismol. Soc. Am.*, *66*(3), 667–675.

Fuis, G. S., T. Ryberg, N. J. Godfrey, D. A. Okaya, and J. M. Murphy (2001), Crustal structure and tectonics from the Los Angeles basin to the Mojave Desert, southern California, *Geology*, *29*(1), 15–18.

Fuis, G. S., et al. (2003), Fault systems of the 1971 San Fernando and 1994 Northridge earthquakes, southern California: Relocated aftershocks and seismic images from LARSE II, *Geology*, *31*(2), 171–174.

Fukahata, Y., and M. Matsu'ura (2005), General expressions for internal deformation fields due to a dislocation source in a multilayered elastic half-space, *Geophys. J. Int.*, *161*(2), 507–521.

Gonzalez, T., and T. K. Rockwell (1991), Holocene Activity of the Springville Fault in Camarillo, Transverse Ranges, Southern California; Preliminary Observations, in *Engineering Geology along the Simi-Santa Rose Fault System and Adjacent Areas, Simi Valley to Camarillo, Ventura County, California; Field Trip Guidebook of the 1991 Annual Field Trip*, edited by T. F. Blake and R. A. Larson, pp. 369–383, Association of Engineering Geologists, Southern California Section.

Griffith, W. A., and M. L. Cooke (2004), Mechanical validation of the three-dimensional intersection geometry between the Puente Hills blind-thrust system and the Whittier fault, Los Angeles, California, *Bull. Seismol. Soc. Am.*, *94*(2), 493–505.

Griffith, W. A., and M. L. Cooke (2005), How sensitive are fault slip rates in the Los Angeles Basin to tectonic boundary conditions?, *Bull. Seismol. Soc. Am.*, *95*(4), 1263–1275.

Griffith, W. A., S. Nielsen, G. Di Toro, and S. A. Smith (2010), Rough faults, distributed weakening, and off-fault deformation, *J. Geophys. Res.*, *115*, B08409, doi:10.1029/2009JB006925.

Hager, B. H., G. A. Lyzenga, A. Donnellan, and D. Dong (1999), Reconciling rapid strain accumulation with deep seismogenic fault planes in the Ventura Basin, California, *J. Geophys. Res.*, *104*(B11), 25,207–225,219.

Herbert, J. W., and M. L. Cooke (2012), Sensitivity of the southern San Andreas fault system to tectonic boundary conditions and fault configurations, *Bull. Seismol. Soc. Am.*, *102*(5), 2046–2062.

Hitchcock, C. S., S. C. Lindvall, J. A. Treiman, K. D. Weaver, J. G. Helms, and W. R. Lettis (2001), Paleoseismic Investigation of the Simi fault, Ventura County, California, 47 pp., *Final Technical Report*, U.S. Geological Survey, Award 01-HQGR0094.

Hooper, A. (2008), A multi-temporal InSAR method incorporating both persistent scatterer and small baseline approaches, *Geophys. Res. Lett.*, *35*, L16302, doi:10.1029/2008GL034654.

Hooper, A., H. Zebker, P. Segall, and B. Kampes (2004), A new method for measuring deformation on volcanoes and other natural terrains using InSAR persistent scatterers, *Geophys. Res. Lett.*, *31*, L23611, doi:10.1029/2004GL021737.

Hooper, A., P. Segall, and H. Zebker (2007), Persistent scatterer interferometric synthetic aperture radar for crustal deformation analysis, with application to Volcán Alcedo Galápagos, *J. Geophys. Res.*, *112*, B07407, doi:10.1029/2006JB004763.

Hudnut, K. W., et al. (1996), Co-seismic displacements of the 1994 Northridge, California Earthquake, *Bull. Seismol. Soc. Am.*, *86*(1B), S19–S36.

Huftile, G. J., and R. S. Yeats (1994), Late Quaternary structure and convergence rates in the coastal Ventura Basin, *AAPG Bull.*, *78*(4), 666.

Huftile, G. J., and R. S. Yeats (1995), Convergence rates across a displacement transfer zone in the western Transverse Ranges, Ventura Basin, California, *J. Geophys. Res.*, *100*(B2), 2043–2067.

Huftile, G. J., and R. S. Yeats (1996), Deformation rates across the Placerita (Northridge M (sub w) = 6 7 aftershock zone) and Hopper Canyon segments of the western Transverse Ranges deformation belt, *Bull. Seismol. Soc. Am.*, *86*(1), 3–18.

Jackson, J., and P. Molnar (1990), Active faulting and block rotations in the Western Transverse Ranges, California, *J. Geophys. Res.*, *95*(B13), 22,073–22,087.

Jolivet, R., R. Cattin, N. Chamot-Rooke, C. Lasserre, and G. Peltzer (2008), Thin-plate modeling of interseismic deformation and asymmetry across the Altyn Tagh fault zone, *Geophys. Res. Lett.*, *35*, L02309, doi:10.1029/2007GL031511.

Kaven, J. O., F. Maerten, and D. D. Pollard (2011), Mechanical analysis of fault slip data: Implications for paleostress analysis, *J. Struct. Geol.*, *33*, 78–91.

Kohler, M. D., H. Magistrale, and R. W. Clayton (2003), Mantle Heterogeneities and the SCEC Reference Three-Dimensional Seismic Velocity Model Version 3, *Bull. Seismol. Soc. Am.*, *93*(2), 757–774.

Lamb, S. (1994), A simple method for estimating the horizontal velocity field in wide zones of active deformation—II. Examples from New Zealand, Central Asia and Chile, *Geophys. J. Int.*, *119*(1), 313–337.

Langbein, J. (2004), Noise in two-color electronic distance meter measurements revisited, *J. Geophys. Res.*, *109*, B04406, doi:10.1029/2003JB002819.

Langbein, J. (2012), Estimating rate uncertainty with maximum likelihood: differences between power-law and flicker–random-walk models, *J. Geod.*, *86*(9), 775–783.

Loveless, J. P., and B. J. Meade (2011), Stress modulation on the San Andreas fault by interseismic fault system interactions, *Geology*, *39*(11), 1035–1038.

Luyendyk, B. P. (1991), A model for Neogene crustal rotations, transtension, and transpression in southern California, *Geol. Soc. Am. Bull.*, *103*(11), 1528–1536.

Luyendyk, B. P., M. J. Kamerling, and R. Terres (1980), Geometric model for Neogene crustal rotations in southern California, *Geol. Soc. Am. Bull.*, *91*(4), 211–217.

Magistrale, H., S. Day, R. W. Clayton, and R. Graves (2000), The SCEC southern California reference three-dimensional seismic velocity model version 2, *Bull. Seismol. Soc. Am.*, *90*(6), S65–S76.

Marshall, S. T., and A. C. Morris (2012), Mechanics, slip behavior, and seismic potential of corrugated dip-slip faults, *J. Geophys. Res.*, *117*, B03403, doi:10.1029/2011JB008642.

Marshall, S. T., M. L. Cooke, and S. E. Owen (2008), Effects of non-planar fault topology and mechanical interaction on fault slip distributions in the Ventura Basin, California, *Bull. Seismol. Soc. Am.*, *98*(3), 1113–1127.

Marshall, S. T., M. L. Cooke, and S. E. Owen (2009), Interseismic deformation associated with three-dimensional faults in the greater Los Angeles region, California, *J. Geophys. Res.*, *114*, B12403, doi:10.1029/2009JB006439.

McCaffrey, R. (2005), Block kinematics of the Pacific-North America plate boundary in the southwestern United States from inversion of GPS, seismological, and geologic data, *J. Geophys. Res.*, *110*, B07401, doi:10.1029/2004JB003307.

Meade, B. J., and B. H. Hager (2005), Block models of crustal motion in Southern California constrained by GPS measurements, *J. Geophys. Res.*, *110*, B03403, doi:10.1029/2004JB003209.

Meade, B. J., B. Hager, S. McClusky, R. Reilinger, S. Ergintav, O. Lenk, A. Barka, and H. Özenwr (2002), Estimates of seismic potential in the Marmara Sea region from block models of secular deformation constrained by Global Positioning System measurements, *Bull. Seismol. Soc. Am.*, *92*(1), 208–215.

Meigs, A. J., M. L. Cooke, and S. T. Marshall (2008), Using vertical rock uplift patterns to infer and validate the three-dimensional fault configuration in the Los Angeles basin, *Bull. Seismol. Soc. Am.*, *98*(2), 106–123.

Menke, W. (1989), *Geophysical Data Analysis: Discrete Inverse Theory*, Academic Press, San Diego, CA.

Namson, J. S., and T. L. Davis (1988), Structural transect of the western Transverse Ranges, California: Implications for lithospheric kinematics and seismic risk evaluation, *Geology*, *16*, 675–679.

Okada, Y. (1985), Surface deformation due to shear and tensile faults in a half-space, *Bull. Seismol. Soc. Am.*, *75*(4), 1135–1154.

Peterson, M. D., and S. G. Wesnousky (1994), Fault slip rates and earthquake histories for active faults in southern California, *Bull. Seismol. Soc. Am.*, *84*(5), 1608–1649.

Peterson, M. D., W. A. Bryant, C. H. Cramer, T. Cao, M. Reichle, A. D. Frankel, J. L. Lienkaemper, P. A. McCrory, and D. P. Schwartz (1996), Probabilistic seismic hazard assessment for the state of California Rep. 96–706, 68 pp, USGS.

Platt, J. P., and T. W. Becker (2010), Where is the real transform boundary in California, *Geochem., Geophys., Geosyst.*, *11*, Q06012, doi:10.1029/2010GC003060.

Plesch, A., et al. (2007), Community Fault Model (CFM) for Southern California, *Bull. Seismol. Soc. Am.*, *97*, 1793–1802.

Ritz, E., and D. D. Pollard (2012), Stick, slip, and opening of wavy frictional faults: A numerical approach in two dimensions, *J. Geophys. Res.*, *117*, B03405, doi:10.1029/2011JB008624.

Rockwell, T. K. (1988), Neotectonics of the San Cayetano Fault, Transverse Ranges, California, *Geol. Soc. Am. Bull.*, *100*(4), 500–513.

Rockwell, T. K., E. A. Keller, M. N. Clark, and D. L. Johnson (1984), Chronology and rates of faulting of Ventura River terraces California, *Geol. Soc. Am. Bull.*, *95*, 1466–1474.

Rubin, C. M., S. C. Lindvall, and T. K. Rockwell (1998), Evidence for large earthquakes in metropolitan Los Angeles, *Science*, *281*, 398–402.

Savage, J. C. (1983), A dislocation model of strain accumulation and release at a subduction zone, *J. Geophys. Res.*, *88*(B6), 4984–4996.

Savage, J. C. (1998), Displacement field for an edge dislocation in a layered half-space, *J. Geophys. Res.*, *103*(B2), 2439–2446.

Savage, J. C., and R. O. Burford (1970), Accumulation of tectonic strain in California, *Bull. Seismol. Soc. Am.*, *60*, 1877–1896.

Savage, J. C., and R. O. Burford (1973), Geodetic determination of relative plate modtion in central California, *J. Geophys. Res.*, *78*(5), 832–845.

Savage, J. C., and M. Lisowski (1998), Viscoelastic coupling model of the San Andreas Faults along the Big Bend, southern California, *J. Geophys. Res.*, *103*(B4), 7281–7292.

Savage, J. C., J. L. Svarc, and W. H. Prescott (1999), Geodetic estimates of fault slip rates in the San Francisco Bay area, *J. Geophys. Res.*, *104*(B3), 4995–5002.

Schmalzle, G., T. H. Dixon, R. Malservisi, and R. Govers (2006), Strain accumulation across the Carrizo segment of the San Andreas Fault, Califnornia: Impact of laterally varying crustal properties, *J. Geophys. Res.*, *111*, B05403, doi:10.1029/2005JB003843.

Scientists of the U.S. Geologic Survey (USGS) and the Southern California Earthquake Center (SCEC) (1994), The Magnitude 6.7 Northridge, California, Earthquake of 17 January 1994, *Science*, *266*(5184), 389–397.

Shaw, B. E., and C. H. Scholz (2001), Slip-length scaling in large earthquakes: observations and theory and implications for earthquake physics, *Geophys. Res. Lett.*, *28*(15), 2995–2998.

Shaw, B. E., and S. G. Wesnousky (2008), Slip-length scaling in large earthquakes: The role of deep-penetrating slip below the seismogenic layer, *Bull. Seismol. Soc. Am.*, *98*(4), 1633–1641.

Shaw, J. H., A. Plesch, J. F. Dolan, T. L. Pratt, and P. Fiore (2002), Puente Hills blind-thrust system, Los Angeles California, *Bull. Seismol. Soc. Am.*, *92*(8), 2946–2960.

Shen, Z., D. D. Jackson, and B. X. Ge (1996), Crustal deformation across and beyond the Los Angeles basin from geodetic measurements, *J. Geophys. Res.*, *101*(B12), 27,957–927-980.

Thomas, A. L. (1993), POLY3D: A three-dimensional, polygonal element, displacement discontinuity boundary element computer program with applications to fractures, faults, and cavities in the Earth's crust, Master's thesis, Stanford University, Stanford, Calif.

Titus, S. J., M. Dyson, C. DeMets, B. Tikoff, F. Rolandone, and R. Bürgmann (2011), Geologic versus geodetic deformation adjacent to the San Andreas fault, central California, *Geol. Soc. Am. Bull.*, *123*(5/6), 794–820.

Tsutsumi, H., and R. S. Yeats (1999), Tectonic setting of the 1971 Sylmar and 1994 Northridge earthquakes in the San Fernando Valley, California, *Bull. Seismol. Soc. Am.*, *89*(5), 1232–1249.

Tsutsumi, H., R. S. Yeats, and G. J. Huftile (2001), Late Cenozoic tectonics of the northern Los Angeles fault system, California, *Geol. Soc. Am. Bull.*, *113*(4), 454–468.

Tucker, A. Z., and J. F. Dolan (2001), Paleoseismologic evidence for a >8 Ka age of the most recent surface rupture on the eastern Sierra Madre fault, northern Los Angeles Metropolitan region, California, *Bull. Seismol. Soc. Am.*, *91*(2), 232–249.

Wald, D. J., T. H. Heaton, and K. W. Hudnut (1996), The slip history of the 1994 Northridge, California, earthquake determined from strong-motion, teleseismic, GPS, and leveling data, *Bull. Seismol. Soc. Am.*, *86*(1B), S49–S70.

Wang, R., F. L. Martín, and F. Roth (2003), Computation of deformation induced by earthquakes in a multi-layered elastic crust—FORTRAN programs EDGRN/EDCMP, *Comput. Geosci.*, *29*(2), 195–207.

Wessel, P., and W. H. F. Smith (1998), New, improved version of the Generic Mapping Tools released, *Eos Trans. AGU*, *79*, 579.

Wright, T. L. (1991), Structural geology and tectonic evolution of the Los Angeles Basin, in *Active Margin Basins*, edited by K. T. Biddle, pp. 35–134, American Association of Petroleum Geologists Memoir 52, California.

Yeats, R. S. (1977), High rates of vertical crustal movement near Ventura, California, *Science*, *196*(4287), 295–298.

Yeats, R. S. (1983), Large-scale Quaternary detachments in Ventura Basin, southern California, *J. Geophys. Res.*, *88*(B1), 569–583.

Yeats, R. S. (1987), Late Cenozoic structure of the Santa Susana fault zone, *U.S. Geol. Surv. Prof. Pap.*, *1339*, 137–160.

Yeats, R. S. (1988), Late Quaternary slip rate on the Oak Ridge Fault, Transverse Ranges, California; implications for seismic risk, *J. Geophys. Res.*, *93*(B10), 12,137–112,149.

Yeats, R. S. (1993), Converging more slowly, *Nature*, *366*(6453), 299–301.

Yeats, R. S., W. H. K. Lee, and R. F. Yerkes (1987), Geology and seismicity of the eastern Red Mountain Fault Ventura County, *U.S. Geol. Surv. Prof. Pap.*, *1339*, 161–167.

Yeats, R. S., G. J. Huftile, and F. B. Grigsby (1988), Oak Ridge Fault, Ventura fold belt, and the Sisar decollement, Ventura Basin, California, *Geology*, *16*(12), 1112–1116.

Zebker, H., and J. Villasenor (1992), Decorrelation in interferometric radar echoes, *IEEE Trans. Geosci. Remote Sens.*, *30*(5), 950–959.